

Targeted protein S-nitrosylation of ACE2 inhibits SARS-CoV-2 infection

Received: 7 March 2022

Accepted: 24 August 2022

Published online: 29 September 2022

 Check for updates

Chang-ki Oh¹, Tomohiro Nakamura¹, Nathan Beutler², Xu Zhang¹, Juan Piña-Crespo¹, Maria Talantova¹, Swagata Ghatak¹, Dorit Trudler¹, Lauren N. Carnevale¹, Scott R. McKercher¹, Malina A. Bakowski³, Jolene K. Diedrich¹, Amanda J. Roberts⁴, Ashley K. Woods³, Victor Chi³, Anil K. Gupta³, Mia A. Rosenfeld⁵, Fiona L. Kearns⁵, Lorenzo Casalino⁵, Namir Shaabani², Hejun Liu⁶, Ian A. Wilson⁶, Rommie E. Amaro⁵, Dennis R. Burton², John R. Yates III¹, Cyrus Becker⁷, Thomas F. Rogers^{2,8}, Arnab K. Chatterjee³ and Stuart A. Lipton^{1,9}✉

Prevention of infection and propagation of severe acute respiratory syndrome coronavirus 2 (SARS-CoV-2) is a high priority in the Coronavirus Disease 2019 (COVID-19) pandemic. Here we describe S-nitrosylation of multiple proteins involved in SARS-CoV-2 infection, including angiotensin-converting enzyme 2 (ACE2), the receptor for viral entry. This reaction prevents binding of ACE2 to the SARS-CoV-2 spike protein, thereby inhibiting viral entry, infectivity and cytotoxicity. Aminoadamantane compounds also inhibit coronavirus ion channels formed by envelope (E) protein. Accordingly, we developed dual-mechanism aminoadamantane nitrate compounds that inhibit viral entry and, thus, the spread of infection by S-nitrosylating ACE2 via targeted delivery of the drug after E protein channel blockade. These non-toxic compounds are active in vitro and in vivo in the Syrian hamster COVID-19 model and, thus, provide a novel avenue to pursue therapy.

The process of SARS-CoV-2 infection first involves binding of the viral spike protein to a cell surface receptor, which has been shown to be ACE2 (ref. ¹). Viral entry into cells can be accomplished by fusion of the viral E protein, located on SARS-CoV-2 near the spike protein, to facilitate fusion with the cell surface, or endocytosis with subsequent envelope fusion to endosomal membranes^{2–4}. We reasoned that using the E protein viroporin channel to target a molecular warhead to the ACE2 receptor to inhibit interaction with the spike protein could yield a novel mechanism for drug action to treat COVID-19.

Along these lines, we built upon our experience in developing the aminoadamantane drug, memantine, as a US Food & Drug Administration-approved treatment for Alzheimer's disease and

synthesized several additional compounds with improved efficacy^{5–9}. These new chemical probes, termed aminoadamantane nitrates, offer dual-allosteric inhibition of the ion channel associated with the *N*-methyl-D-aspartate (NMDA) type of glutamate receptor in the brain, with the aminoadamantane moiety providing channel block as well as targeted delivery of a nitric oxide (NO)-related group to S-nitrosylate, and, thus, further inhibit the receptor. Moreover, these aminoadamantane nitrates have displayed no untoward side effects, such as hypotension or other NO-associated actions, in two-species toxicity studies^{5–9}. Intriguingly, aminoadamantane drugs such as amantadine and memantine were originally developed as antiviral agents because they also block the ion channel found in the envelope of multiple

¹Departments of Molecular Medicine and Neuroscience, Neurodegeneration New Medicines Center, La Jolla, CA, USA. ²Department of Immunology and Microbiology, Scripps Research Institute, La Jolla, CA, USA. ³Calibr, a division of the Scripps Research Institute, La Jolla, CA, USA. ⁴Animal Models Core, Scripps Research Institute, La Jolla, CA, USA. ⁵Department of Chemistry and Biochemistry, University of California, San Diego, La Jolla, CA, USA. ⁶Department of Integrative Structural and Computational Biology, Scripps Research Institute, La Jolla, CA, USA. ⁷EuMentis Therapeutics, Inc., Newton, MA, USA. ⁸Division of Infectious Diseases, Department of Medicine, University of California, San Diego, La Jolla, CA, USA. ⁹Department of Neurosciences, School of Medicine, University of California, San Diego, La Jolla, CA, USA. ✉e-mail: slipton@scripps.edu

viruses, including influenza and the β -coronaviruses, and anecdotal reports in humans suggest that they may possibly offer some efficacy for SARS-CoV-2, but definitive data are lacking^{2,3,10–14}. Coupled with the facts that SARS-CoV and SARS-CoV-2 have also been shown to be susceptible to NO, in part by inhibiting their protease and replication cycle¹⁵, and NO-based therapies have shown promise in human clinical trials for COVID-19 treatment¹⁶, we postulated that the new aminoadamantane nitrate drugs might provide mechanistic information on the mode of action of NO against SARS-CoV-2 and offer improved antiviral activity. Indeed, we show here that the aminoadamantane moiety can block the ion channel in the envelope of SARS-CoV-2 to provide a guided missile to target a therapeutic warhead to ACE2 and, thus, prevent interaction with the nearby spike protein. Accordingly, we demonstrate that the viral receptor, ACE2, can be S-nitrosylated by NO-related species generated by the nitro adduct of the aminoadamantane nitrate compounds to inhibit viral entry.

Results

S-Nitrosylated ACE2 inhibits binding to SARS-CoV-2 spike protein

Initially, we investigated the molecular mechanism whereby NO-related species might inhibit SARS-CoV-2 activity. As assessed by biotin switch assay, we found that the host cell membrane protein receptor for SARS-CoV-2, ACE2, and a protease that cleaves the viral spike protein, transmembrane serine protease 2 (TMPRSS2), both of which are necessary for viral entry and infectivity^{1,17}, could be S-nitrosylated by the physiological small molecule NO donor and transnitrosylating

agent S-nitrosocysteine (SNOC) (Fig. 1a–c). Interestingly, multiple cysteine residues have been shown to be of importance in ACE2 and TMPRSS2 activity, so S-nitrosylation might be expected to disrupt their activity^{18,19}.

We focused on S-nitrosylation of ACE2 (forming SNO-ACE2), reasoning that this nitrosylation reaction might prevent binding of SARS-CoV-2 S protein to ACE2, thus inhibiting viral infection. To test this premise, we exposed HeLa cells stably expressing human ACE2 (HeLa-ACE2) to SNOC and assessed SNO-ACE2 formation by biotin switch assay. To evaluate binding of the spike protein to these HeLa-ACE2 cells, we then incubated the cells with purified recombinant SARS-CoV-2 spike protein (S1 + S2). Because NO dissipates very quickly from SNOC (<5 minutes at neutral pH), and spike protein was added sequentially after this period, we could rule out the possibility of direct S-nitrosylation of spike protein by SNOC under these conditions. We found that the formation of SNO-ACE2 was stable for at least 12 hours (Extended Data Fig. 1). The receptor-binding domain (RBD) in the S1 subunit of the SARS-CoV-2 spike glycoprotein binds to ACE2 expressed on the surface of host cells, whereas the C-terminal S2 membrane anchoring subunit functions to translocate virus into host cells^{19,20}. After pre-incubation of HeLa-ACE2 cells with SNOC, we found significantly decreased binding of purified spike protein to HeLa-ACE2 cells (Fig. 1d,e), consistent with the notion that the cysteine residue(s) susceptible to S-nitrosylation in ACE2 affected spike protein binding.

Human ACE2 protein contains eight cysteine residues, six of which participate in formation of three pairs of disulfide bonds, and the

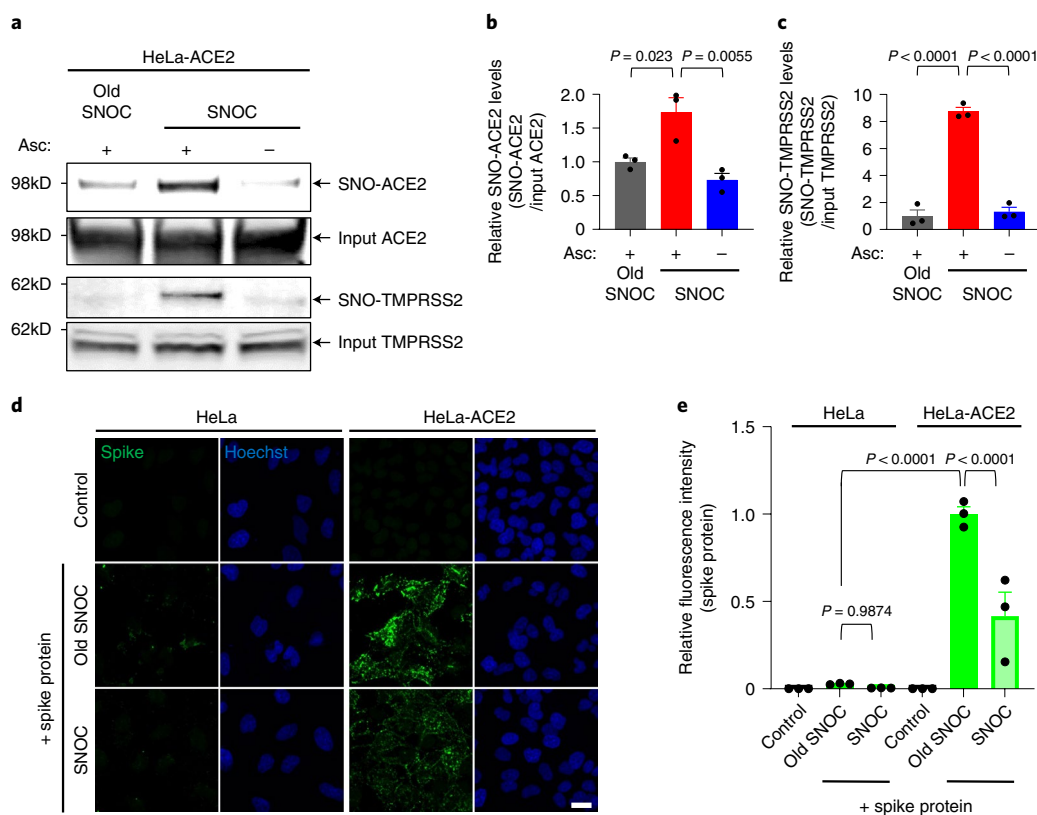


Fig. 1 | SNOC increases S-nitrosylation of ACE2 and inhibits binding of SARS-CoV-2 spike protein. **a**, Assay for SNO-ACE2 and SNO-TMPRSS2 in HeLa-ACE2 cells. Cells were exposed to 100 μ M SNOC or, as a control, 'old' SNOC (from which NO had been dissipated). After 20 minutes, cell lysates were subjected to biotin switch assay to assess SNO and input (total) proteins detected by immunoblotting with cognate antibody. The ascorbate minus (Asc-) sample served as a negative control. **b,c**, Ratio of SNO-ACE2/input ACE2 protein and SNO-TMPRSS2/input TMPRSS2 protein. Data are mean + s.e.m. by one-way

ANOVA with Tukey's multiple comparisons. $n = 3$ biological replicates. **d**, HeLa and HeLa-ACE2 cells were pre-exposed to 100 μ M SNOC or old SNOC. After 30 minutes, 10 μ g ml⁻¹ of purified recombinant SARS-CoV-2 spike (S1 + S2) protein was incubated with the cells. After 1 hour, cells were fixed with 4% PFA for 15 minutes, and bound spike protein was detected by anti-spike protein antibody; nuclei were stained with Hoechst. Scale bar, 20 μ m. **e**, Quantification of relative fluorescence intensity. Data are mean + s.e.m. by two-way ANOVA with Tukey's multiple comparisons. $n = 3$ biological replicates.

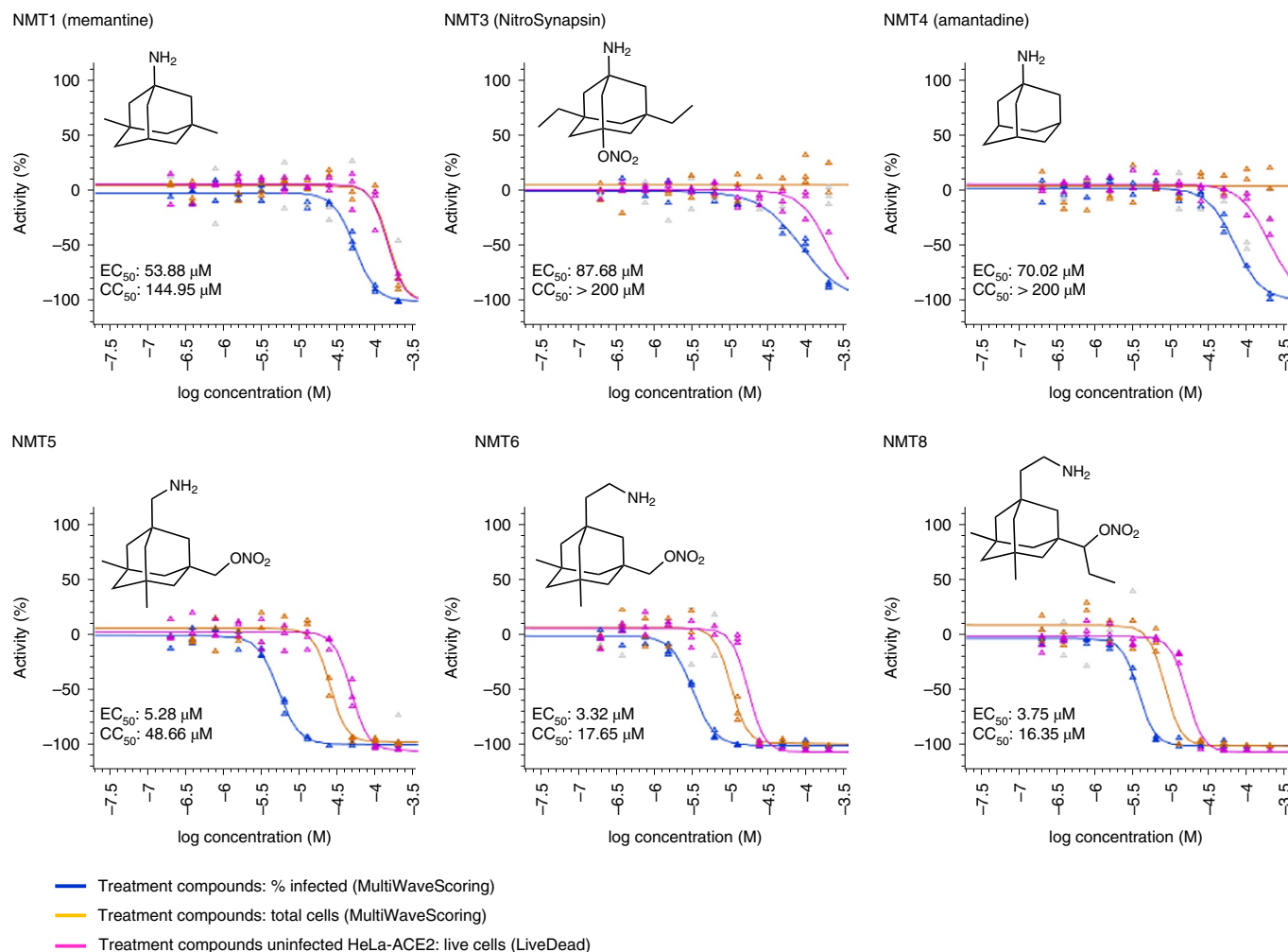


Fig. 2 | Dose response of drugs screened against SARS-CoV-2. Dose–response curves showing the EC₅₀ of each compound against SARS-CoV-2 (% infected cells, blue), total cell counts (orange) in the infection experiment and the CC₅₀ for

uninfected host cell toxicity (magenta), as assessed in HeLa-ACE2 cells. See also Supplementary Dataset 1 for the full dataset.

remaining two (Cys²⁶¹ and Cys⁴⁹⁸) are present as free thiols (or thiolates) (Extended Data Fig. 2a)¹⁹ and, thus, potentially available for S-nitrosylation via reversible nucleophilic attack on a nitroso nitrogen to form an SNO-protein adduct²¹. Accordingly, we performed site-directed mutagenesis of these cysteine residues in ACE2 and found that C261A, C498A or C261A/C498A mutation significantly inhibited SNO-mediated S-nitrosylation on biotin switch assays, consistent with the notion that these two cysteine residues are targets of S-nitrosylation (Extended Data Fig. 2b,c). Moreover, mass spectrometry confirmed the presence of S-nitrosylated ACE2 at Cys²⁶¹ and Cys⁴⁹⁸ after exposure to SNO (Extended Data Fig. 2d).

SNO-ACE2 destabilizes dimerization and spike protein binding

Notably, these S-nitrosylation sites on ACE2 are located near the collectrin-like domain (CLD) region rather than the spike protein-binding domain region (Extended Data Fig. 3a). This suggests that S-nitrosylation may affect the conformation of ACE2 protein at some distance from the S-nitrosylated cysteine residue(s) to diminish binding of ACE2 to trimeric spike protein^{19,20,22}. Accordingly, explicitly solvated, all-atom molecular dynamics simulations of the SNO-ACE2/RBD complex in plasma membrane show that the distance between each SNO-ACE2 protomer's center of mass (COM) is overall much longer and more broadly distributed than in simulations of wild-type (WT) ACE2 dimer (Extended Data Fig. 3a,b)²². This behavior indicates

a certain extent of destabilization of the dimer interface imparted by S-nitrosylation, particularly of C⁴⁹⁸. Specifically, at the beginning of the simulations, the SNO-ACE2/RBD model displays a hydrogen bond between Q175_A and Q139_B, which is then interchanged with D136_B (Extended Data Fig. 3c). This is the only interaction between the peptidase domains (PDs) of the two protomers, as also reported for the initial cryogenic electron microscopy (cryo-EM) structure²³. Notably, over the course of our simulations, this interaction was progressively lost (Extended Data Fig. 3d), leading to partial disruption of the PD dimeric interface and transient detachment of the two protomers. Therefore, we hypothesize that the addition of S-nitrosylation at the sidechain of C⁴⁹⁸, which is located in the vicinity of Q¹⁷⁵, could be sufficient to induce rearrangement in the packing of secondary structural elements of this region, leading, in turn, to the disruption of the only point of contact between the two PDs of ACE2. The loss of this contact may potentially trigger a further destabilization at the level of the dimeric interface between the neck domains. Alteration of ACE2 dimer stability has the potential to interfere with the SARS-CoV-2 spike binding²⁴, thus abrogating infection.

Screening aminoadamantane nitrate compounds against SARS-CoV-2 infection

Next, we examined the effect of aminoadamantane nitrate compounds on SARS-CoV-2 entry into cells, causing infection. Aminoadamantanes

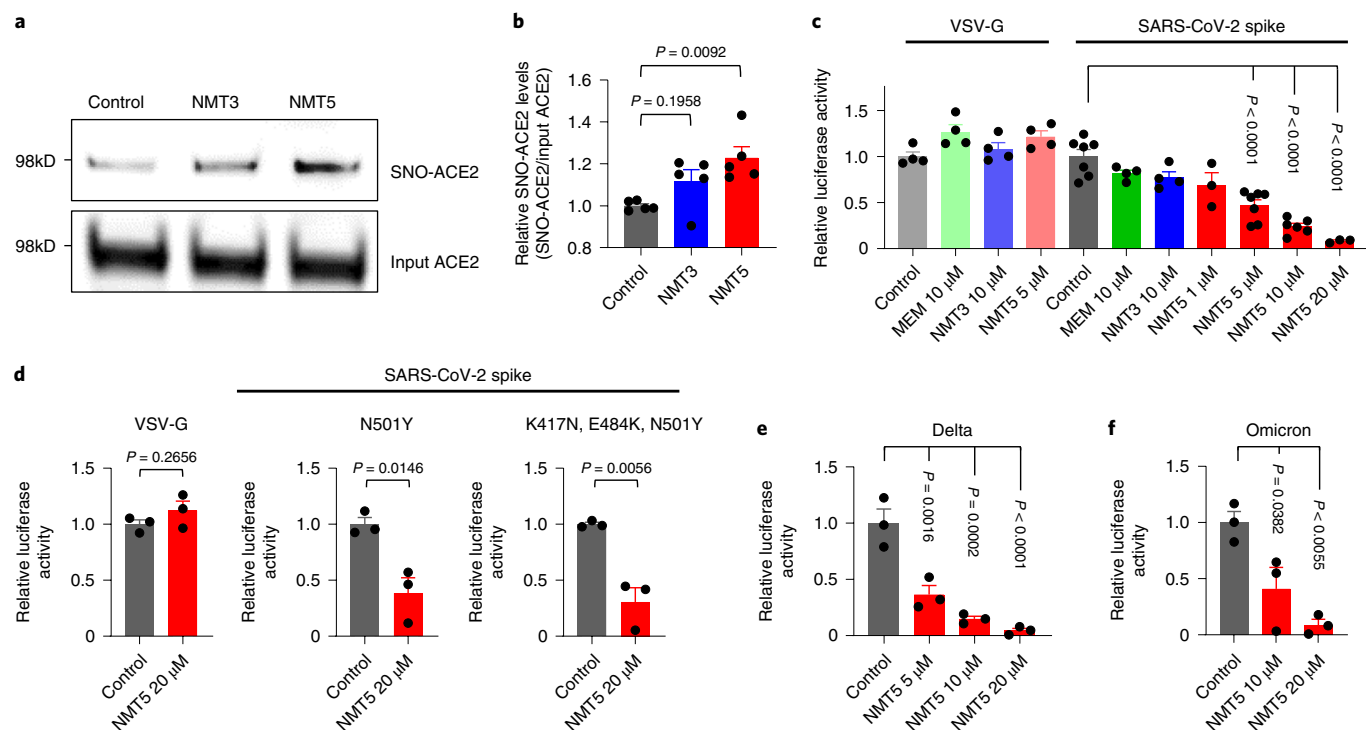


Fig. 3 | NMT5 inhibits SARS-CoV-2 pseudoviral entry. a, HeLa-ACE2 cells were treated with 10 μ M NMT3 or 5 μ M NMT5. After 1 hour, cell lysates were subjected to biotin switch assay for protein S-nitrosylation, detected by immunoblotting with anti-ACE2 antibody. **b**, Ratio of SNO-ACE2/input ACE2 protein. Data are mean \pm s.e.m. by one-way ANOVA with Tukey's multiple comparisons. $n = 5$ biological replicates. **c**, HeLa-ACE2 cells were incubated with SARS-CoV-2 spike (D614) or VSV-G (control) pseudovirus particles in the presence and absence of MEM (memantine), NMT3 or NMT5. After 48 hours, viral transduction efficiency was monitored by luciferase activity. Data are mean \pm s.e.m. by one-way ANOVA

with Tukey's multiple comparisons. $n = 3$ –7 biological replicates. **d–f**, HeLa-ACE2 cells were incubated in the presence and absence of NMT5 with SARS-CoV-2 N501Y spike, SARS-CoV-2 K417N/E484K/N501Y spike or VSV-G (control) pseudovirus particles (**d**) or with SARS-CoV-2 Delta variant (**e**) or Omicron variant pseudovirus particles (**f**). After 48 hours, viral transduction efficiency was monitored by luciferase activity. Data are mean \pm s.e.m. by two-tailed Student's *t*-test (**d**) or one-way ANOVA with Tukey's for multiple comparisons (**e,f**). $n = 3$ biological replicates.

have been reported to directly bind to the viroporin ion channel formed by the SARS-CoV-2 E protein^{10,25,26}. Therefore, we screened our series of aminoadamantane and nitro-aminoadamantane compounds^{6–8} as potential therapeutic drugs against SARS-CoV-2. These latter chemical probes might be expected to bind to the viral channel, thus targeting S-nitrosylation to ACE2 to inhibit its interaction with spike protein and, thus, viral entry. Specifically, we tested, in a masked fashion, the efficacy against live SARS-CoV-2 in HeLa-ACE2 cells of aminoadamantanes (memantine, blindly coded as NMT1, and amantadine/NMT4) and aminoadamantane nitrate compounds (NMT2, NMT3 and NMT5-NMT9) (Fig. 2 and Extended Data Fig. 4; full dataset shown in Supplementary Dataset 1). As positive controls, we used remdesivir, apilimod and puromycin (Supplementary Dataset 1)^{27,28}. In determining the therapeutic potential of these compounds, we considered the selectivity index (SI) that compares a compound's half-maximal non-specific cytotoxicity (CC_{50}) in the absence of infection to its half-maximal effective antiviral concentration (EC_{50}) (CC_{50}/EC_{50}) (Supplementary Dataset 1). The SI can be considered an *in vitro* indicator of therapeutic index and, ideally, would approach 10. The aminoadamantane compounds alone (amantadine and memantine) offered no efficacy and, thus, were not studied further. In contrast, several of the aminoadamantane nitrate compounds offered some degree of protection from infection. However, NMT6 and NMT8 may have done this simply by killing the host cells irrespective of infection, as evidenced by its off-target killing of uninfected cells in the live/dead assay (Fig. 2 and Supplementary Dataset 1). Among the seven aminoadamantane nitrate compounds tested, NMT5 displayed the best combination of EC_{50} and CC_{50} (SI = 9.2) with an EC_{50} for protection against SARS-CoV-2 of 5.28 μ M (Fig. 2 and Supplementary

Dataset 1); this concentration of compound is well within the micromolar amounts attainable in human tissues at well-tolerated doses, as tested in two animal species^{6–9,29}. Additionally, NMT3 (also known as NitroSynapsin), which was already being developed for central nervous system indications^{6–9}, displayed some degree of protection against SARS-CoV-2 with an EC_{50} of 87.7 μ M, although this value may be artificially high due to the short half-life of NMT3 in aqueous solution under *in vitro* conditions^{6,9,30}. Hence, these two compounds were advanced for further study. We next asked if NMT3 and NMT5 could S-nitrosylate ACE2. We found that NMT5 > NMT3 effectively S-nitrosylated ACE2 both *in vitro* in HeLa-ACE2 cells and *in vivo* in Syrian hamsters, as assessed by the biotin switch assay (Fig. 3a,b and Extended Data Fig. 5). Notably, a statistically significant increase in the level of S-nitrosylated ACE2 was observed in the SARS-CoV-2 target tissues of lung and kidney at 48 hours after oral administration of a single dose of drug at 10 mg kg⁻¹ (Extended Data Fig. 5d–i). Consistent with the structure–activity relationship indicating that SNO-ACE2 was associated with the antiviral effect of NMT5 and NMT3, the other aminoadamantane nitrates (including NMT6 and NMT8) did not S-nitrosylate ACE2 at low micromolar concentrations (Extended Data Fig. 6).

SNO-ACE2 inhibits SARS-CoV-2 variant infectivity

Because we had found that S-nitrosylation of ACE2 inhibited the binding of SARS-CoV-2 spike protein, we next asked if NMT3-mediated or NMT5-mediated SNO-ACE2 formation could prevent viral entry into host cells. To test this premise, we employed a replication-deficient Maloney murine leukemia virus (MLV)-based SARS-CoV-2 spike protein pseudotyped virus, initially using the most prevalent strain of spike

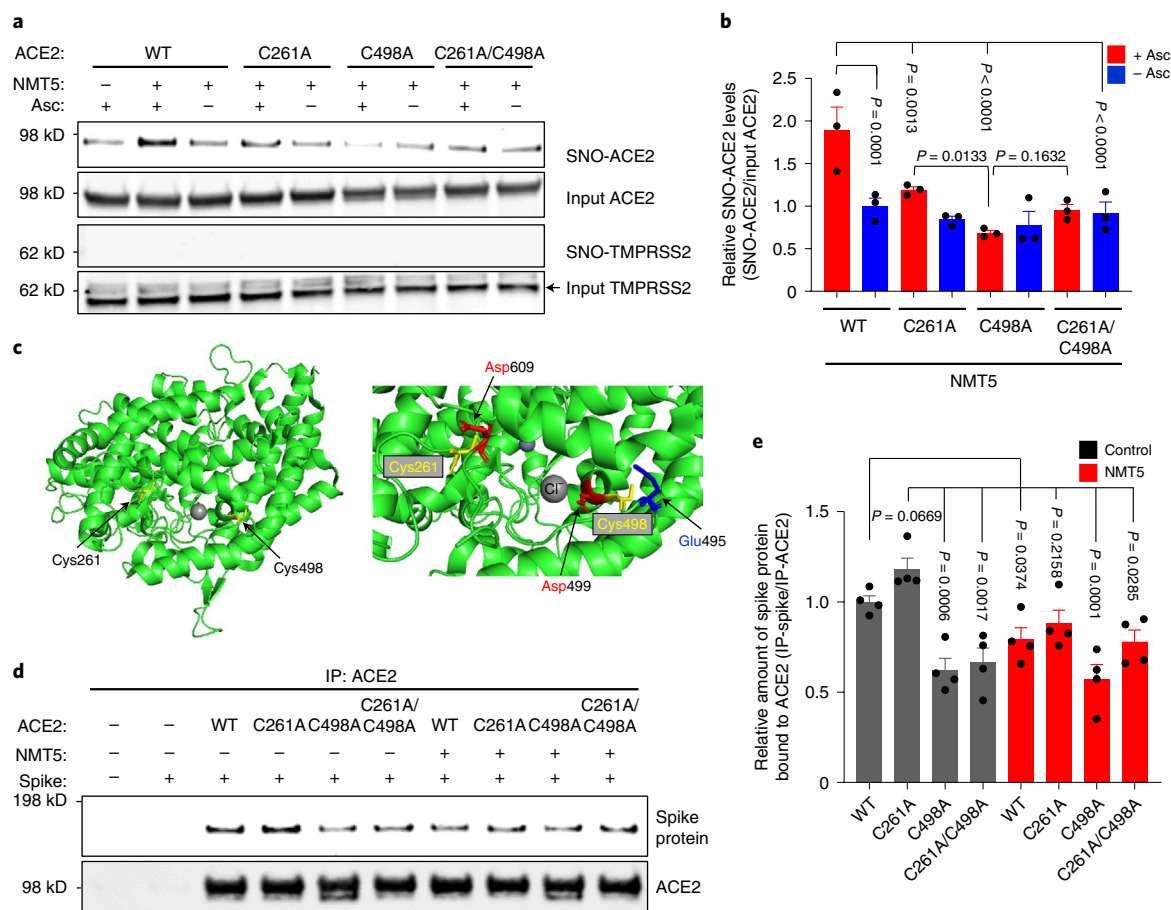


Fig. 4 | S-Nitrosylation of ACE2 by NMT5 inhibits binding to spike protein.

a, HEK293T cells were transfected with plasmids encoding human WT ACE2 or non-nitrosylatable mutant ACE2 (C262A, C498A or C261A/C498A). Cells were treated with 10 μ M NMT5 and subjected to biotin switch assay for detection of S-nitrosylated proteins by immunoblotting with anti-ACE2 and anti-TMPRSS2 antibodies. The absence of ascorbate (Asc⁻) served as a negative control.

b, Ratio of SNO-ACE2/input ACE2. Data are mean \pm s.e.m. by two-way ANOVA with Fisher's LSD multiple comparisons. $n = 3$ biological replicates. **c**, Crystal structure of ACE2 (left panel; PDB ID: 6MOJ) with enlarged view of S-nitrosylation sites of

ACE2. Glu⁴⁹⁵ and Asp⁴⁹⁹, acidic amino acid residues, surround Cys⁴⁹⁸ (right panel).

d, HEK293T cells were transfected with plasmids encoding human WT ACE2 or non-nitrosylatable mutant ACE2 (C262A, C498A or C261A/C498A). Cells were exposed to 1 μ g ml⁻¹ of purified recombinant SARS-CoV-2 spike protein in the presence or absence of 5 μ M NMT5; after 1 hour, cells were lysed and subjected to co-IP with anti-ACE2 antibody. Immunoprecipitated ACE2 and spike protein were detected by immunoblotting with anti-ACE2 and anti-spike protein antibodies.

e, Ratio of IP-ACE2/IP-spike protein. Data are mean \pm s.e.m. by one-way ANOVA with Fisher's LSD multiple comparisons. $n = 4$ biological replicates.

protein (D614) as of early 2020 (ref. ³¹). We examined whether NMT3 and NMT5 could suppress infection with this SARS-CoV-2 pseudovirus. We found that NMT5 inhibited SARS-CoV-2 pseudoviral entry in a dose-dependent manner, with 5 μ M inhibiting 53%, 10 μ M inhibiting 76% and 20 μ M inhibiting 92% (Fig. 3c). NMT3 showed more limited ability to suppress pseudovirus entry, ~24% at 10 μ M. The fact that S-nitrosylation of ACE2 manifested inhibition in the pseudovirus assay (as shown in Fig. 3c) at approximately the same EC₅₀ of 5 μ M as found in the live virus infection assay (Fig. 2) strongly implies that SNO-ACE2 formation is indeed the predominant mechanism by which NMT5 prevents viral infection. As a control, the NMT5 metabolite lacking the nitro group did not suppress SARS-CoV-2 infection in the pseudovirus entry assay (Fig. 3c and Extended Data Fig. 7). As a further control, the pseudovirus entry assay performed with vesicular stomatitis virus G protein (VSV-G) was unaffected by NMT3 or NMT5 (Fig. 3c).

We next examined if NMT5 could suppress viral infection from more recently identified SARS-CoV-2 variants, including N501Y spike protein, a common mutation in B.1.1.7 (or Alpha variant, United Kingdom) and B.1.351 (or Beta variant, South Africa), and P.1 (or Gamma variant, Brazil), encountered in the winter of 2020/2021. Additionally, we tested K417N, E484K and N501Y spike protein, as found in the B.1.351 and P.1 variants, the B.1.617.2 variant (or Delta, Indian; T19R, G142D,

156/157 DELETION, R158G, L452R, T478K, D614G, P681R and D950N) and the BA.1 variant (or Omicron, South Africa), found in 2021/2022, which are associated with higher transmissibility or severity as well as altered antigenicity³². We found that NMT5 was also effective in reducing infectivity of these SARS-CoV-2 variants, including the Delta and Omicron variants, by up to 95% (Fig. 3d–f). These results are consistent with the notion that NMT5 \gg NMT3-mediated S-nitrosylation of ACE2 can inhibit SARS-CoV-2 entry into host cells.

NMT5-induced SNO-ACE2 inhibits spike protein binding

Next, we sought to determine if NMT5 could modify ACE2 at both of the cysteine residues (Cys²⁶¹ and Cys⁴⁹⁸) that we demonstrated to be susceptible to S-nitrosylation by SNO. Analysis by cysteine mutation revealed that NMT5 preferentially S-nitrosylated Cys⁴⁹⁸ over Cys²⁶¹ (Fig. 4a,b). Interestingly, the crystal structure of ACE2 shows that an acid/base motif (comprised of Glu⁴⁹⁵ and Asp⁴⁹⁹), which, under some conditions, may facilitate S-nitrosylation, is present near Cys⁴⁹⁸, whereas only a partial motif (represented by Asp⁶⁰⁹) is found near Cys²⁶¹ (Fig. 4c)^{33–35}. This observation is consistent with previous findings that potent or supraphysiological amounts of NO, donors such as SNO, can S-nitrosylate cysteine residues surrounded by no motif or only a partial SNO motif³⁰, whereas a full SNO motif can facilitate S-nitrosylation by less potent

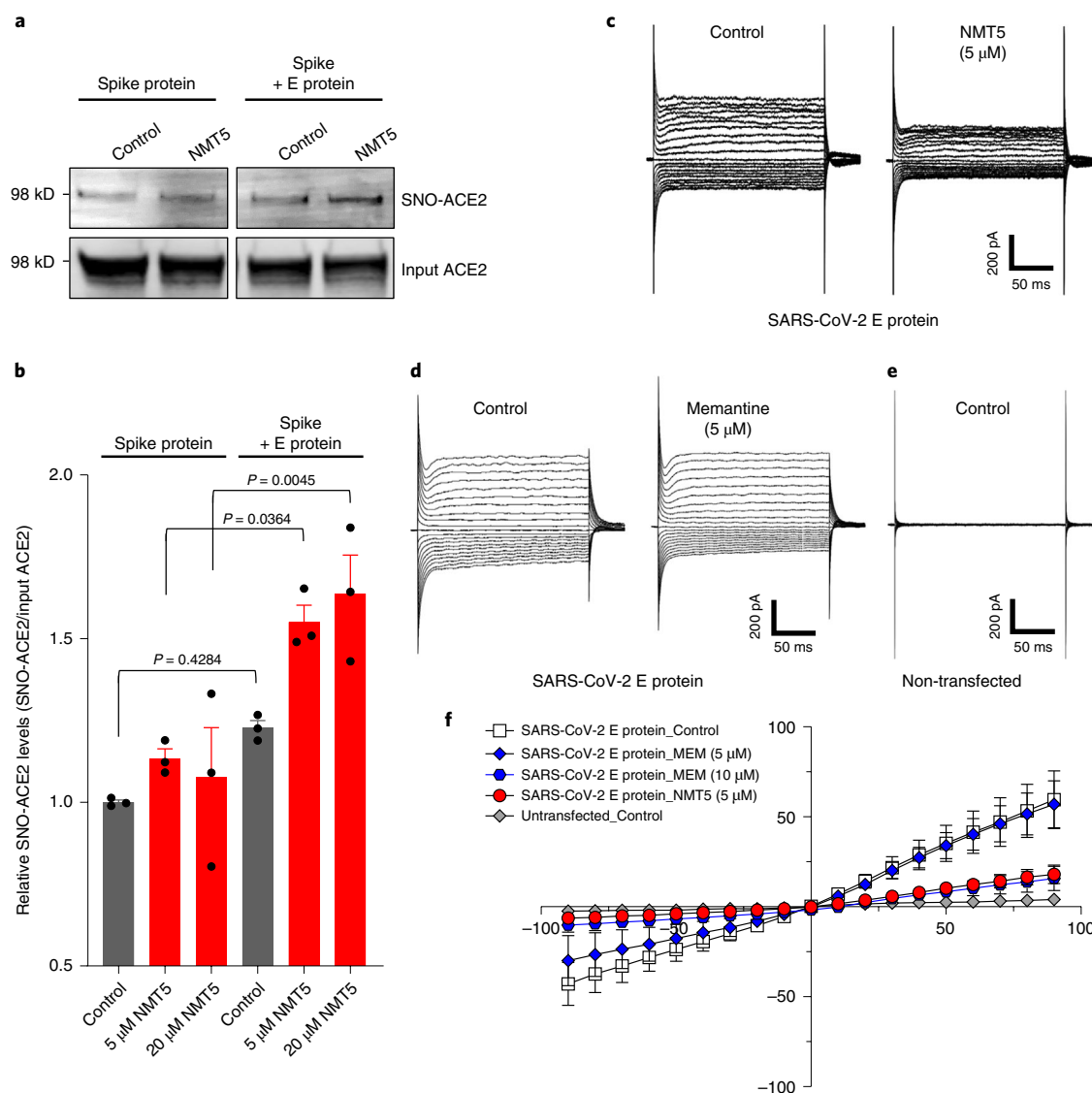


Fig. 5 | Targeted S-nitrosylation of ACE2 and inhibition of E viroporin protein channel by NMT5. a, E protein plasmid was transiently transfected into HEK293T-spike protein cells. After 1 day, cells were harvested and plated onto HeLa-ACE2 cells in the presence or absence of 5 μ M NMT5. After 30 minutes, cell lysates were subjected to biotin switch assay to monitor protein S-nitrosylation of ACE2, detected by immunoblotting. **b**, Ratio of SNO-ACE2/total input ACE2 protein. Data are mean \pm s.e.m. by two-way ANOVA with Tukey's multiple comparisons. $n = 3$ biological replicates. **c–e**, Representative traces of whole-cell currents from

untransfected ($n = 4$) and transiently transfected ($n = 15$) HEK293T cells before and after application of memantine or NMT5 during patch-clamp recording. Whole-cell currents were generated by holding cells at 0 mV and applying voltage steps between -90 mV and $+90$ mV in increments of 10 mV. **f**, Current-voltage (I - V) curves from steady-state current density (pA/pF) versus holding potential (mV) for memantine (MEM, 5 μ M and 10 μ M) and NMT5 (5 μ M). Data are mean \pm s.e.m.; $n = 16$ cells recorded.

donors, presumably like NMT5. Mechanistically, cysteine thiol groups (in fact, thiolates) are nucleophiles that can perform reversible nucleophilic attack on an electrophilic nitroso nitrogen^{36,37}. The local environment of the thiolate anion can kinetically favor one electrophile over another; moreover, the bulky R-group of NMT5, as an RNOx donor ($x = 1$ or 2) compared to the small molecule SNOc, could sterically hinder reactivity³⁰. Notably, concentrations of NMT5 that significantly inhibited viral entry (~ 10 μ M) failed to S-nitrosylate other proteins, including TMPRSS2, spike protein or E protein (Fig. 4a and Extended Data Fig. 8), demonstrating relative selectivity of NMT5 for ACE2 at the cell surface. Although we cannot rule out the possibility that proteins associated with virus intracellular trafficking are S-nitrosylated, this would be less likely as aminoadamantane nitrate compounds are known to act on extracellular rather than intracellular targets^{5–9}.

To further investigate the effect of NMT5 on SARS-CoV-2 spike protein binding to ACE2, we performed co-immunoprecipitation

(co-IP) experiments of these two proteins in the presence and absence of NMT5 using anti-ACE2 antibody for IP. As expected, the two proteins co-immunoprecipitated, as evidenced on immunoblots. NMT5 (5 μ M) diminished this co-IP, consistent with the notion that the compound could inhibit binding of spike protein to ACE2 to a significant degree (Fig. 4d,e). As controls, the spike protein was not co-immunoprecipitated with cysteine mutant ACE2(C498A) or with double mutant ACE2(C261A/C498A) to a significant level, although mutant ACE2(C261A) was still co-immunoprecipitated. These data suggest that S-nitrosylation predominantly of C⁴⁹⁸ of ACE2 is important for spike protein binding to ACE2. Moreover, NMT5 inhibited co-IP of the spike protein and ACE2(C261A) while having less effect on mutant ACE2(C498A) or ACE2(C261A/C498A) binding (Fig. 4d,e). Thus, the co-IP experiment suggests that the intact Cys residue is needed for full interaction/binding of spike protein with ACE2. Either Cys mutation or S-nitrosylation can significantly decrease the interaction of spike

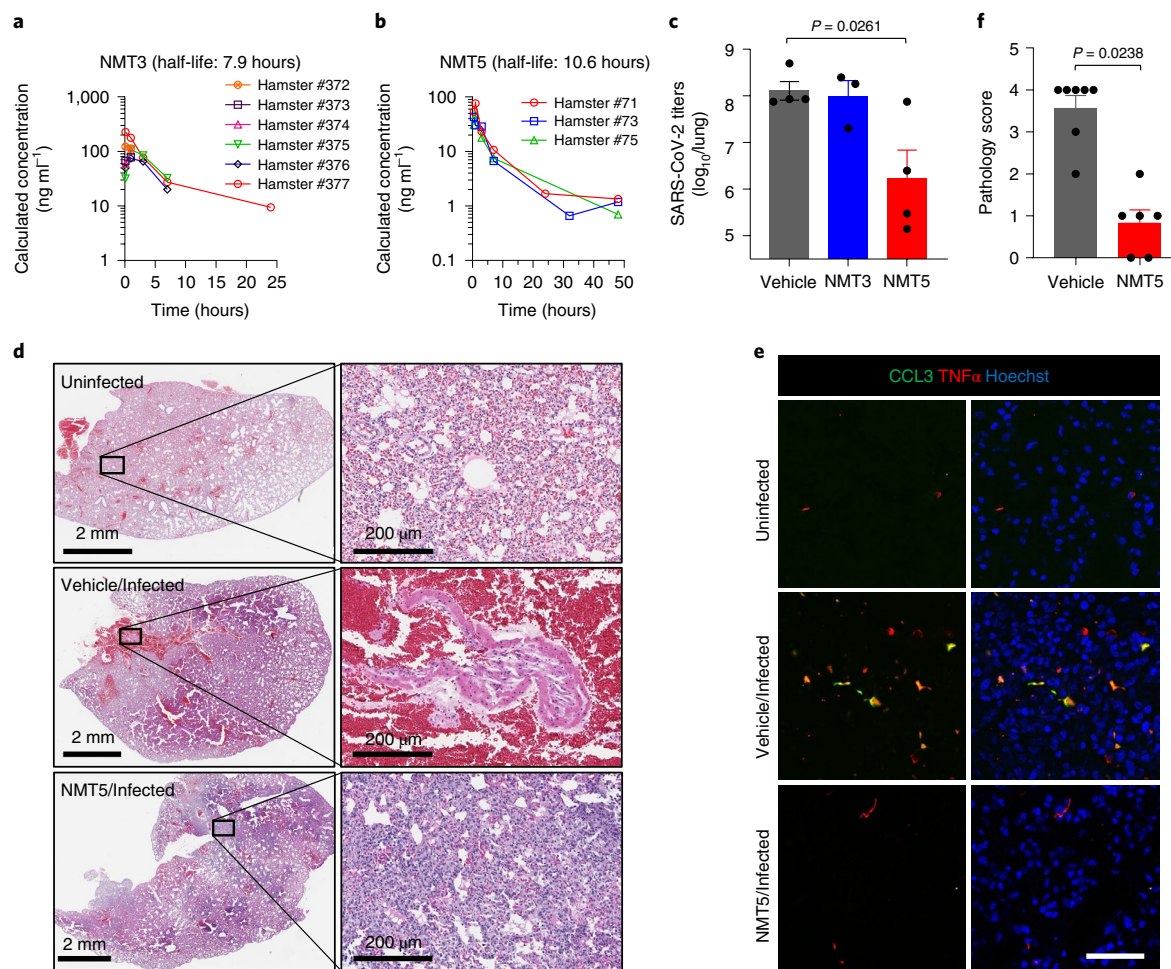


Fig. 6 | NMT5 inhibits SARS-CoV-2 infection in vivo in Syrian hamsters. a, b, PK data in plasma for NMT3 ($n = 6$) and NMT5 ($n = 3$) in Syrian hamsters after an oral dose of 10 mg kg^{-1} . **c,** Live viral load in Syrian hamsters monitored by plaque assay from lung tissue 2 days after infection after treatment with NMT3, NMT5 or vehicle (Control). Data are mean + s.e.m. by two-tailed Student's t -test ($n = 8$ Syrian hamsters tested). **d, e,** Syrian hamsters were sacrificed 5 days after infection with SARS-CoV-2 that were either untreated (labeled Vehicle/Infected) or treated with oral NMT5 (NMT5/Infected) and compared to control (Uninfected). Representative H&E-stained sections showed virtually no areas of large hemorrhage (confluent bright red regions) in NMT5-treated hamster lungs

compared to vehicle-treated. Scale bars, 2 mm; high magnification $200 \mu\text{m}$ (**d**). Representative immunohistochemistry of lung sections stained with anti-TNF α cytokine antibody and anti-CCL3 (MIP-1 α) chemokine antibody from untreated and NMT5-treated hamsters 5 days after SARS-CoV-2 infection; uninfected sections are shown as a control. Merged image with Hoechst stain for DNA shown in right-hand panels. Scale bar, $40 \mu\text{m}$ (**e**). **f,** Lung pathology scores (Methods) for infected hamsters, either untreated or treated with NMT5. Treated hamsters showed significant improvement. Data are mean + s.e.m. by two-tailed Mann–Whitney U -test ($n = 9$ Syrian hamsters tested).

protein with ACE2. Taken together, these results are consistent with the notion that NMT5 inhibits SARS-CoV-2 spike protein from binding to ACE2 and, thus, virus entry into the cell via S-nitrosylation of ACE2.

NMT5 targets SNO to ACE2 via blockade of the E protein channels

Intriguingly, we found that the presence of the E protein of SARS-CoV-2 appeared to target S-nitrosylation by NMT5 to nearby ACE2 receptor proteins (Fig. 5a,b and Extended Data Fig. 9). To investigate this action further, we assessed the ability of the aminoadamantane compound, memantine, and the lead aminoadamantane nitrate candidate, NMT5, to block ion channel activity of the E protein¹¹ using the patch-clamp technique. To test direct interaction with the viroporin channel, we transiently transfected HEK293T cells with a construct encoding the E protein and assessed voltage-dependent currents (versus uninfected cells) in the presence and absence of drug (Fig. 5c–f). Under our conditions, we found that the presence of the E protein resulted in a robust voltage-dependent current carried by K^+ that was inhibited by memantine and with greater potency by NMT5. Notably, the low micromolar

concentrations needed to see these effects are within attainable levels in mammalian plasma and tissues, as shown in pharmacokinetic (PK) studies, and have proven to be safe in animal toxicity studies^{6–9,29}.

NMT5 protects from SARS-CoV-2 infection in vivo

In preparation for in vivo efficacy testing of our chemical probes in a COVID-19 small animal model, we next performed 48-hour PK studies after a single oral dose of NMT3 or NMT5 at 10 mg kg^{-1} in ~150-g Syrian hamsters. We found a half-life in plasma for NMT3 of 7.9 hours and for NMT5 of 10.6 hours (Fig. 6a,b and Supplementary Table 1). The mean C_{max} for NMT5 was $0.2 \mu\text{M}$ and $0.4 \mu\text{M}$ for NMT3; NMT3 also displayed a hydroxylated metabolite (full detailed PK dataset shown in Supplementary Datasets 2 and 3). The fact that NMT5 was found to be more stable than NMT3 by mass spectrometry analysis (Fig. 6a,b and Supplementary Table 1) was also consistent with previous findings^{6–9,29}. Moreover, these drugs are concentrated in tissues up to ~30-fold over plasma levels. Using a Bayesian-like adaptive clinical trial design, we determined the maximal tolerated dose (MTD) of NMT3 and NMT5 in vivo based on dose-ranging toxicity and efficacy studies in 52 Syrian hamsters. To assess treatment

efficacy in the Syrian hamster model of COVID-19 at the MTD for NMT5, we administered by oral gavage 200 mg kg⁻¹ in two equally divided doses separated by 12 hours, with the initial dose timed right after challenge with the virus and the second dose 12 hours later^{31,38}. Based on the PK results, at this dose, drug levels in tissue should approach or exceed the EC₅₀ found in our in vitro screens to significantly decrease viral infectivity. We found in the Syrian hamster model that this regimen of NMT5, but not NMT3, knocked down live viral titers of SARS-CoV-2 after infection by ~100-fold, as measured by plaque assay (Fig. 6c). In the absence of depletion by antibodies^{31,39}, virus can persist in lung tissue for several days even in the absence of infection and, thus, contribute to plaque assay titers; any significant decrement is encouraging as a potential treatment. More importantly in this model is the histological examination of the lungs for large hemorrhages related to actual SARS-CoV-2 infection, reflecting direct blood vessel damage as also seen in human lungs with fatal COVID-19 (ref. 40). In this regard, on histological examination, NMT5 virtually eliminated large COVID-19-related hemorrhages in the lungs of infected hamsters compared to vehicle when examined up to 5 days after infection (Fig. 6d). This translational model revealed a striking absence of large SARS-CoV-2-induced hemorrhages in the lungs of NMT5-treated hamsters versus controls, with all controls displaying such hemorrhages, whereas no NMT-5 treated animals did so ($n = 12$; $P < 0.01$ by Fisher's exact test)⁴¹. The lethal effect of large hemorrhagic conversion was completely prevented by NMT5. Although some inflammatory changes were noted in the NMT5-treated lung tissue compared to uninfected controls, it was far less than in the infected/untreated tissue (Fig. 6d). In fact, pro-inflammatory cytokine and chemokine activation downstream of infection were abated with NMT5 treatment compared to vehicle control, as demonstrated by immunohistochemical staining of lung sections (Fig. 6e). Quantification of these results in an overall pathology score showed significant protection by NMT5 (Fig. 6f). These findings benchmark favorably against our group's published studies on the same model using antibodies directed against spike protein^{31,39}.

Discussion

In summary, development of an oral drug to combat acute SARS-CoV-2 infection remains a high priority to treat the COVID-19 pandemic, particularly for the unvaccinated segment of the world population. Our findings provide proof of concept that the cellular receptor of SARS-CoV-2, ACE2, can be S-nitrosylated. This nitrosylation reaction appears to inhibit binding of SARS-CoV-2 spike protein, thus inhibiting viral entry, infectivity and cytotoxicity. As emerging evidence for this mechanism of action, our binding, co-IP and Cys mutation experiments show a significant degree of disruption of binding of spike protein to ACE2 after S-nitrosylation of ACE2 or after mutation of the S-nitrosylation sites on ACE2. In fact, this mechanism was predicted in our molecular dynamics (MD) simulation experiments. We acknowledge, however, that, although this is a rational explanation, it remains a hypothesis for the observed mechanism of viral inhibition by chemical probes that S-nitrosylate ACE2.

Taking advantage of these findings, we developed a novel aminoadamantane nitrate compound, NMT5, as a chemical probe that provides inhibition of SARS-CoV-2 activity by protein S-nitrosylation. NMT5 contains a nitro group, and we provide evidence that this nitro group is targeted to ACE2 by aminoadamantane-mediated viroporin channel blockade of the E protein^{2,3,10–12}. The discovery that ACE2 could be S-nitrosylated was quite unexpected, as most authorities had postulated that the beneficial effects of NO on patients with COVID-19 was due to a direct effect on the virus itself. These mechanistic insights provided by our chemical probes should facilitate development of aminoadamantane nitrate drugs for acute antiviral therapy for human COVID-19.

A key concept of this novel approach to ameliorating infection by SARS-CoV-2 is that these nitro-aminoadamantane compounds may

prevent the viral spike protein from binding to the ACE2 receptor by S-nitrosylating the receptor in targeted fashion, apparently facilitated by blockade of the vicinal viroporin E protein (Fig. 5 and Extended Data Figs. 9 and 10). Hence, drugs like NMT5 should also prevent new variants of the spike protein from binding to ACE2 because ACE2 itself is blocked. In this manner, the development of aminoadamantane nitrates for COVID-19 drug therapy complements other drug, vaccine and antibody therapies, which are dependent on spike protein antigenic sites and, thus, may eventually be susceptible to evasion by further spike protein mutation. Critically, the binding of NMT5 to the viroporin channel may also confer the ability to block spread of SARS-CoV-2 from one host to another. To explain this mechanistically, we posit that NMT5 binds to the E protein viroporin channel on SARS-CoV-2 and then transfers NO to ACE2 on the host cell to prevent infection (Fig. 5a,b and Extended Data Fig. 9). However, if a patient is already infected and takes an NMT5-like drug, the newly produced viral particles will bind to the aminoadamantane moiety of NMT5 via their E protein viroporin channels; hence, viral infectivity should be limited when a new potential host is exposed to this virus because the new host's ACE2 target protein will be S-nitrosylated by the drug attached to the viral particles as the virus approaches ACE2 on the new host. Compounds like NMT5 thus provide tools for the development of a novel strategy to combat spread of COVID-19 from one host to another.

Online content

Any methods, additional references, Nature Research reporting summaries, source data, extended data, supplementary information, acknowledgements, peer review information; details of author contributions and competing interests; and statements of data and code availability are available at <https://doi.org/10.1038/s41589-022-01149-6>.

References

- Hoffmann, M. et al. SARS-CoV-2 cell entry depends on ACE2 and TMPRSS2 and is blocked by a clinically proven protease inhibitor. *Cell* **181**, 271–280 (2020).
- Kozakov, D., Chuang, G. Y., Beglov, D. & Vajda, S. Where does amantadine bind to the influenza virus M2 proton channel? *Trends Biochem. Sci.* **35**, 471–475 (2010).
- Torres, J. et al. Conductance and amantadine binding of a pore formed by a lysine-flanked transmembrane domain of SARS coronavirus envelope protein. *Protein Sci.* **16**, 2065–2071 (2007).
- Asarnow, D. et al. Structural insight into SARS-CoV-2 neutralizing antibodies and modulation of syncytia. *Cell* **184**, 3192–3204 (2021).
- Lipton, S. A. Paradigm shift in neuroprotection by NMDA receptor blockade: memantine and beyond. *Nat. Rev. Drug Discov.* **5**, 160–170 (2006).
- Wang, Y. et al. The pharmacology of aminoadamantane nitrates. *Curr. Alzheimer Res.* **3**, 201–204 (2006).
- Talantova, M. et al. Aβ induces astrocytic glutamate release, extrasynaptic NMDA receptor activation, and synaptic loss. *Proc. Natl Acad. Sci. USA* **110**, E2518–E2527 (2013).
- Tu, S. et al. NitroSynapsin therapy for a mouse MEF2C haploinsufficiency model of human autism. *Nat. Commun.* **8**, 1488 (2017).
- Takahashi, H. et al. Pharmacologically targeted NMDA receptor antagonism by NitroMemantine for cerebrovascular disease. *Sci. Rep.* **5**, 14781 (2015).
- Pervushin, K. et al. Structure and inhibition of the SARS coronavirus envelope protein ion channel. *PLoS Pathog.* **5**, e1000511 (2009).
- Schoeman, D. & Fielding, B. C. Coronavirus envelope protein: current knowledge. *Viol. J.* **16**, 69 (2019).
- Nieva, J. L., Madan, V. & Carrasco, L. Viroporins: structure and biological functions. *Nat. Rev. Microbiol.* **10**, 563–574 (2012).

13. Mandala, V. S. et al. Structure and drug binding of the SARS-CoV-2 envelope protein transmembrane domain in lipid bilayers. *Nat. Struct. Mol. Biol.* **27**, 1202–1208 (2020).
14. Butterworth, R. F. Potential for the repurposing of adamantane antivirals for COVID-19. *Drugs R D* **21**, 267–272 (2021).
15. Akaberi, D. et al. Mitigation of the replication of SARS-CoV-2 by nitric oxide in vitro. *Redox Biol.* 101734 (2020).
16. Adusumilli, N. C., Zhang, D., Friedman, J. M. & Friedman, A. J. Harnessing nitric oxide for preventing, limiting and treating the severe pulmonary consequences of COVID-19. *Nitric Oxide* **103**, 4–8 (2020).
17. Li, Y. et al. SARS-CoV-2 and three related coronaviruses utilize multiple ACE2 orthologs and are potently blocked by an improved ACE2-Ig. *J. Virol.* **94**, e01283–20 (2020).
18. Thunders, M. & Delahunt, B. Gene of the month: TMPRSS2 (transmembrane serine protease 2). *J. Clin. Pathol.* **73**, 773–776 (2020).
19. Cai, Y. et al. Distinct conformational states of SARS-CoV-2 spike protein. *Science* **369**, 1586–1592 (2020).
20. Huang, Y., Yang, C., Xu, X. F., Xu, W. & Liu, S. W. Structural and functional properties of SARS-CoV-2 spike protein: potential antiviral drug development for COVID-19. *Acta Pharmacol. Sin.* **41**, 1141–1149 (2020).
21. Nakamura, T. et al. Noncanonical transnitrosylation network contributes to synapse loss in Alzheimer's disease. *Science* **371**, eaaw0843 (2021).
22. Barros, E. P. et al. The flexibility of ACE2 in the context of SARS-CoV-2 infection. *Biophys. J.* **120**, 1072–1084 (2020).
23. Yan, R. et al. Structural basis for the recognition of SARS-CoV-2 by full-length human ACE2. *Science* **367**, 1444–1448 (2020).
24. Casalino, L. et al. AI-driven multiscale simulations illuminate mechanisms of SARS-CoV-2 spike dynamics. *Int. J. High Perform. Comput. Appl.* <https://journals.sagepub.com/doi/10.1177/10943420211006452> (2021).
25. Singh Tomar, P. P. & Arkin, I. T. SARS-CoV-2 E protein is a potential ion channel that can be inhibited by gliclazide and memantine. *Biochem. Biophys. Res. Commun.* **530**, 10–14 (2020).
26. Wilson, L., Gage, P. & Ewart, G. Hexamethylene amiloride blocks E protein ion channels and inhibits coronavirus replication. *Virology* **353**, 294–306 (2006).
27. Wang, M. et al. Remdesivir and chloroquine effectively inhibit the recently emerged novel coronavirus (2019-nCoV) in vitro. *Cell Res.* **30**, 269–271 (2020).
28. Ou, X. et al. Characterization of spike glycoprotein of SARS-CoV-2 on virus entry and its immune cross-reactivity with SARS-CoV. *Nat. Commun.* **11**, 1620 (2020).
29. Okamoto, S. et al. Balance between synaptic versus extrasynaptic NMDA receptor activity influences inclusions and neurotoxicity of mutant huntingtin. *Nat. Med.* **15**, 1407–1413 (2009).
30. Stomberski, C. T., Hess, D. T. & Stamler, J. S. Protein S-nitrosylation: determinants of specificity and enzymatic regulation of S-nitrosothiol-based signaling. *Antioxid. Redox Signal.* **30**, 1331–1351 (2019).
31. Rogers, T. F. et al. Isolation of potent SARS-CoV-2 neutralizing antibodies and protection from disease in a small animal model. *Science* **369**, 956–963 (2020).
32. Funk, T. et al. Characteristics of SARS-CoV-2 variants of concern B.1.1.7, B.1.351 or P.1: data from seven EU/EEA countries, weeks 38/2020 to 10/2021. *Eur. Surveill.* **26**, 2100348 (2021).
33. Lan, J. et al. Structure of the SARS-CoV-2 spike receptor-binding domain bound to the ACE2 receptor. *Nature* **581**, 215–220 (2020).
34. Stamler, J. S., Toone, E. J., Lipton, S. A. & Sucher, N. J. (S)NO signals: translocation, regulation, and a consensus motif. *Neuron* **18**, 691–696 (1997).
35. Greco, T. M. et al. Identification of S-nitrosylation motifs by site-specific mapping of the S-nitrosocysteine proteome in human vascular smooth muscle cells. *Proc. Natl Acad. Sci. USA* **103**, 7420–7425 (2006).
36. Smith, B. C. & Marletta, M. A. Mechanisms of S-nitrosothiol formation and selectivity in nitric oxide signaling. *Curr. Opin. Chem. Biol.* **16**, 498–506 (2012).
37. Lancaster, J. R. Jr. How are nitrosothiols formed de novo in vivo? *Arch. Biochem. Biophys.* **617**, 137–144 (2017).
38. Chan, J. F. et al. Simulation of the clinical and pathological manifestations of Coronavirus Disease 2019 (COVID-19) in golden Syrian hamster model: implications for disease pathogenesis and transmissibility. *Clin. Infect. Dis.* **71**, 2428–2446 (2020).
39. Cho, H. et al. Bispecific antibodies targeting distinct regions of the spike protein potentially neutralize SARS-CoV-2 variants of concern. *Sci. Transl. Med.* **13**, eabj5413 (2021).
40. D'Agnillo, F. et al. Lung epithelial and endothelial damage, loss of tissue repair, inhibition of fibrinolysis, and cellular senescence in fatal COVID-19. *Sci. Transl. Med.* **13**, eabj7790 (2021).
41. Doi, M., Takahashi, F. & Kawasaki, Y. Bayesian noninferiority test for 2 binomial probabilities as the extension of Fisher exact test. *Stat. Med.* **36**, 4789–4803 (2017).

Publisher's note Springer Nature remains neutral with regard to jurisdictional claims in published maps and institutional affiliations.

Springer Nature or its licensor holds exclusive rights to this article under a publishing agreement with the author(s) or other rightsholder(s); author self-archiving of the accepted manuscript version of this article is solely governed by the terms of such publishing agreement and applicable law.

© The Author(s), under exclusive licence to Springer Nature America, Inc. 2022

Methods

Cell lines

HEK293T (System Biosciences, LV900A-1) and HEK293-spike cells (SARS-CoV-2 spike (D614)-expressing 293 cells (293-SARS2-S cells, InvivoGen)) were maintained in DMEM with GlutaMAX (DMEM, high glucose, GlutaMAX Supplement, Life Technologies, 10566016) supplemented with 10% FBS (Sigma-Aldrich, F7524), 100 IU ml⁻¹, and 100 µg ml⁻¹ of penicillin–streptomycin (Thermo Fisher Scientific, 10378016) at 37 °C in a 5% CO₂ incubator. Transfections were carried out with Lipofectamine 2000 (Life Technologies, 11668019) using the protocol recommended by the manufacturer. HeLa-ACE2 cells were a gift from David Nemazee (Scripps Research Institute)³¹. Monkey Vero E6 cells (American Type Culture Collection, CRL-1586) were maintained in complete DMEM (Corning, 15-013-CV) containing 10% FBS, 1× penicillin–streptomycin (Corning, 20-002-CL) and 2 mM L-glutamine (Corning, 25-005-CL) at 37 °C in a 5% CO₂ incubator.

Plasmids

hACE2 was a gift from Hyeryun Choe (Addgene plasmid, 1786; <http://n2t.net/addgene:1786>; RRID: Addgene_1786)⁴². The C262A, C498A and C261/498A mutant ACE2 constructs were generated using the QuikChange Lightning Multi Site-Directed Mutagenesis Kit (Agilent Technologies, 210514), according to the manufacturer's protocol. pGBW-m4252984 (SARS-CoV-2 E) was a gift from Ginkgo Bioworks (Addgene plasmid, 153898; <http://n2t.net/addgene:153898>; RRID: Addgene_153898). MLV-gag/pol, MLV-CMV-luciferase, SARS-CoV-2 and VSV-G plasmids were a gift from David Nemazee (Scripps Research Institute)³¹.

Aminoadamantane and aminoadamantane nitrate drugs

Aminoadamantane nitrate compounds (blindly coded NMT2, NMT3, NMT5-NMT9 and NMT5-met (metabolite, sans nitro group)) were synthesized by and obtained from EuMentis Therapeutics and have been described previously^{6–9,29}. Additionally, note that these compounds were prepared as hydrochloride salts to increase stability and aqueous solubility. The aminoadamantane compounds, memantine and amantadine (blindly coded NMT1 and NMT4), were also obtained from EuMentis Therapeutics. Detailed protocols for chemical synthesis are provided in the Supplementary Note in the Supplementary Information. All compounds were sent to the Scripps Research Institute for testing in a masked fashion, and compound identities were not revealed until after experiments were completed and analyzed.

Biotin switch assays and immunoblotting

For analysis of S-nitrosylated proteins, we performed the biotin switch assay as previously described⁴³. In brief, cells or tissue samples were lysed with HENTS buffer (100 mM HEPES, pH 7.4, 1 mM EDTA, 0.1 mM neocuproine, 0.1% SDS and 1% Triton X-100) containing 10 mM methyl methanethiosulfonate (MMTS). SDS solution (25% w/v) was added to lysed samples to a final concentration of 1% and incubated for 20 minutes at 45 °C with frequent vortexing to facilitate blockade of free thiol groups. After removing excess MMTS by acetone precipitation, S-nitrosothiols were reduced to thiols with 20 mM ascorbate. Newly formed thiols were then linked with the sulfhydryl-specific biotinylating reagent N-[6-(biotinamido)-hexyl]-I'-[2'-(pyridyldithio)] propionamide (biotin-HPDP; Dojindo, SB17-10). Unreacted biotin-HPDP was removed by acetone precipitation, and the pellet was resuspended in HENS buffer (100 mM HEPES, pH 7.4, 1 mM EDTA, 0.1 mM neocuproine and 1% SDS), neutralized and centrifuged to clear any undissolved debris. Five percent of the supernatant was used as the input for the loading control. Biotinylated proteins were pulled down with High Capacity NeutrAvidin Agarose beads (Thermo Fisher Scientific, 29202) and analyzed by immunoblotting for S-nitrosylated ACE2, TMPRSS2 or spike protein. Protein samples were subjected to Bolt Bis-Tris Plus (Thermo Fisher Scientific, NW04122BOX) gel electrophoresis and

transferred to PVDF membranes (Millipore, IPFL00010). Membranes were blocked with Odyssey blocking buffer (Li-Cor, 927-40000) for 30 minutes at room temperature and then probed with primary antibodies against ACE2 (1:3,000, Abcam, ab15348; 1:3,000, Proteintech, 21115-1-AP), TMPRSS2 (1:1,000, Santa Cruz Biotechnology, sc-515727) or SARS-CoV-2 spike protein (1:2,000, Abcam, ab275759). After incubation with secondary antibodies (IR-dye 680LT-conjugated goat anti-mouse (1:20,000; Li-Cor, 926-68020) or IR-dye 800CW-conjugated goat anti-rabbit (1:15,000; Li-Cor, 926-32211)), membranes were scanned with an Odyssey infrared imaging system (Li-Cor). Image Studio (Li-Cor) software was used for densitometric analysis of immunoblots.

Immunocytochemistry for SARS-CoV-2 spike protein

Purified recombinant SARS-CoV-2 spike (S1+S2) protein (10 µg ml⁻¹, Sino Biological, 40589-V08B1) exposed cells were fixed with 4% paraformaldehyde (PFA) for 15 minutes at room temperature, washed three times with PBS and blocked (3% BSA and 0.3% Triton X-100 in PBS) for 30 minutes at room temperature. Cells were incubated with anti-SARS-CoV-2 spike protein antibodies (1:200, Sino Biological, 40150-R007) overnight at 4 °C, followed by incubation with Alexa Fluor 488-conjugated secondary antibody (Thermo Fisher Scientific, A21206). Cells were counterstained with 1 µg ml⁻¹ of Hoechst dye 33342 (Invitrogen). Cell images were acquired with a Nikon A1 confocal microscope using a ×20/0.75 air objective (1-µm Z-stack). Maximum intensity projection of images was generated with NIS-Elements AR, and fluorescence intensity was analyzed with ImageJ software (<https://imagej.nih.gov/ij/download.html>) as previously described⁴⁴.

Expression and purification of human ACE2 protein

The N-terminal peptidase domain of human ACE2 (residues 19–615, GenBank: [BAB40370.1](https://www.ncbi.nlm.nih.gov/nuclot/BAB40370.1)) was cloned into pHCMV3 vector and fused with C-terminal His-tag. The plasmid was transiently transfected into Expi293F cells using ExpiFectamin 293 Reagent (Thermo Fisher Scientific) according to the manufacturer's instructions. The supernatant was collected at day 7 after transfection. The His-tagged ACE2 protein was then purified by Ni-NTA (Qiagen) affinity purification, followed by size-exclusion chromatography. The ACE2 preparation then was buffer-exchanged to 1× PBS for the S-nitrosylation assay.

Co-IP experiments

Cultured cells were harvested and lysed in 1% Triton X-100 in PBS. Equivalent protein quantities were immunoprecipitated with anti-ACE2 antibody (Abcam, ab15348)-conjugated magnetic beads (Dynabeads Protein A; Thermo Fisher Scientific, 10002D) for 90 minutes at room temperature. Immunoprecipitants were eluted and subjected to immunoblotting with anti-ACE2 antibody (1:1,000, Cell Signaling Technology, 15983) and anti-SARS-CoV-2 spike protein antibody (1:2,000, Abcam, ab275759).

Mass spectrometry analysis of S-nitrosylated ACE2 protein

Biotin switch was performed as described above. Biotinylated proteins were then precipitated with iced acetone, pelleted and solubilized in HENS buffer (100 mM HEPES, pH 7.4, 1 mM EDTA, 0.1 mM neocuproine and 1% SDS). The samples were desalted using a ZebaSpin desalting column (Thermo Fisher Scientific) pre-equilibrated with PBS, and biotinylated ACE2 protein was immunoprecipitated as described above. Immunoprecipitated ACE2 was eluted in 1% SDS solution and precipitated using methanol-chloroform. Dried pellets were dissolved in 8 M urea/100 mM triethylammonium bicarbonate (TEAB, pH 8.5). Samples were diluted to 2 M urea/100 mM TEAB, and proteins were trypsin digested overnight at 37 °C. The digested ACE2 peptides were enriched a second time by biotin-avidin affinity to enrich biotinylated peptides representing the initial SNO sites. After avidin enrichment, peptides were eluted by reduction using tris(2-carboxyethyl)phosphine (TCEP).

Samples were analyzed on an Orbitrap Eclipse mass spectrometer (Thermo Fisher Scientific). Samples were injected directly onto a 25-cm, 100- μ m ID column packed with ethylene bridged hybrid (BEH) 1.7- μ m C18 resin (Waters). Samples were separated at a flow rate of 300 nl min⁻¹ on an nLC 1200 (Thermo Fisher Scientific) using a gradient of solution A (0.1% formic acid in water and 5% acetonitrile) and solution B (80% acetonitrile and 0.1% formic acid). Specifically, a gradient of 1–25% B over 100 minutes, an increase to 40% B over 20 minutes, an increase to 100% B over another 10 minutes and held at 90% B for 10 minutes was used for a 140-minute total run time. Peptides were eluted directly from the tip of the column and nanosprayed directly into the mass spectrometer by application of 2.5 kV voltage at the back of the column. The Orbitrap Eclipse mass spectrometer was operated in data-dependent mode. Full MS1 scans were collected in the Orbitrap at 120,000 resolution. The cycle time was set to 3 seconds, and, within these 3 seconds, the most abundant ions per scan were selected for high-energy collisional dissociation (HCD) with detection in the Orbitrap. Monoisotopic precursor selection was enabled, and dynamic exclusion was used with exclusion duration of 5 seconds.

Protein and peptide identification were done with Integrated Proteomics Pipeline-IP2 (Integrated Proteomics Applications). Tandem mass spectra were extracted from raw files using RawConverter⁴⁵ and searched with ProLuCID⁴⁶ against the UniProt human database. The search space included all fully-tryptic and half-tryptic peptide candidates. Data were searched with 50-p.p.m. precursor ion tolerance and 600-p.p.m. fragment ion tolerance. Identified proteins were filtered to 10-p.p.m. precursor ion tolerance using DTASelect⁴⁷ using a target-decoy database search strategy to control the false discovery rate to 1% at the protein level⁴⁸.

MD simulations

The fully glycosylated, Cys²⁶¹/Cys⁴⁹⁸-S-nitrosylated model of human ACE2 dimer bound to two SARS-CoV-2 spike RBDs (with a 1:1 stoichiometry) is based on the cryo-EM structure of the ACE2/RBD/BOAT1 complex (Protein Data Bank (PDB) ID: 6M17)²³. BOAT1 dimer chaperone coordinates were manually removed, and N-glycans were added on both ACE2 and RBD in the same fashion as in Barros et al.²². The sidechain of Cys²⁶¹ and Cys⁴⁹⁸ was S-nitrosylated in both ACE2 protomers using Schrödinger Maestro (Schrödinger Release 2020-4). ParamChem web interface was used to generate CHARMM36 suitable parameters for the S-N = O moiety^{49–51}. The glycosylated and S-nitrosylated ACE2/RBD construct was inserted into a lipid bilayer patch of 350 Å × 350 Å with a composition similar to that of mammalian cell membranes (56% POPC, 20% CHL, 11% POPI, 9% POPE and 4% PSM)^{52,53}. Finally, the resulting system was embedded into an orthorhombic box of explicit waters and Na⁺/Cl⁻ ions at a concentration of 150 mM. MD simulations were performed on the Frontera supercomputer at the Texas Advanced Supercomputing Center using NAMD 2.14 (ref. ⁵⁴) and CHARMM36m all-atom additive force fields^{55,56}. Excluding initial minimization and equilibration, a total of 310 ns were collected for analysis. We note that, except for Cys²⁶¹ and Cys⁴⁹⁸ S-nitrosylation, the model described here is the same as the ACE2/RBD complex presented in Barros et al.²². Therefore, we refer to that work for a complete description of system setup procedures and simulation protocol.

Analysis of COM distance was performed with the compute_center_of_mass function within MDTraj⁵⁷. COM for each ACE2 protomer was calculated taking into account the amino acid backbones of residues 18–742. The distance between COMs was evaluated at each frame along a 310-ns trajectory for both the WT ACE2/RBD complex by Barros et al.²² and the model of the SNO-ACE2/RBD complex presented here. As a reference, the distance between COMs from the cryo-EM structure (PDB ID: 6M17) was also calculated. The simulations were visually inspected using VMD⁵⁸.

SARS-CoV-2 virus generation

Monkey Vero E6 cells were plated in a T225 flask with complete DMEM containing 10% FBS, 1× penicillin–streptomycin, 2 mM L-glutamine and incubated for overnight at 37 °C in a humidified atmosphere of 5% CO₂. The medium in the flask was removed, and 2 ml of complete DMEM containing the WA1 strain of SARS-CoV-2 (USA-WA1/2020 (BEI Resources, NR-52281)) was added to the flask at a multiplicity of infection (MOI) of 0.5. After incubation for 30 minutes at 34 °C in a 5% CO₂ incubator, 30 ml of complete DMEM was added to the flask. The flask was then placed in a 34 °C incubator with 5% CO₂ for 5 days. On day 5 after infection, the supernatant was harvested and centrifuged at 1,000g for 5 minutes. The supernatant was filtered through a 0.22- μ m filter and stored at –80 °C.

SARS-CoV-2/HeLa-ACE2 high-content imaging assay for infection

Control compounds solvated in DMSO were transferred into 384-well μ Clear-bottom plates (Greiner, 781090-2B) using the ADS Labcyte Echo liquid handler. Aminoadamantane and aminoadamantane nitrate compounds to be screened were solvated in saline solution on ice immediately before use and transferred into the assay plates in 5 μ l of DMEM with 2% FBS (assay medium). HeLa-ACE2 cells were added to plates in assay medium at a density of 1.0×10^3 cells per well to a 13- μ l volume. Plated cells were transported to the Biosafety Level 3 facility at Scripps Research Institute, and, within 1 hour, 13 μ l of SARS-CoV-2 diluted in assay media was added at MOI = 0.65. Cells were incubated for 24 hours at 34 °C in a 5% CO₂ incubator and then fixed with 8% formaldehyde for 1 hour. Human polyclonal sera diluted at 1:500 in Perm/Wash buffer (BD Biosciences, 554723) were added to the plate and incubated at room temperature for 2 hours. Then, 6 μ g ml⁻¹ of goat anti-human H+L conjugated Alexa Fluor 488 (Thermo Fisher Scientific, A11013) together with 8 μ M of Antifade DAPI (Thermo Fisher Scientific, D1306) in SuperBlock T20 (PBS) buffer (Thermo Fisher Scientific, 37515) were added to the plate and incubated at room temperature for 1 hour in the dark. Four fields were imaged per well using the ImageXpress Micro Confocal High-Content Imaging System (Molecular Devices) with a $\times 10$ objective. Images were analyzed using the Multi-Wavelength Cell Scoring Application Module (MetaXpress) where DAPI staining was used to identify host cell nuclei (the total number of cells in the images) and the SARS-CoV-2 immunofluorescence signal for identification of infected cells.

Uninfected host cell cytotoxicity counterscreen

Compounds were prepared and plated in 384-well plates as for the infection assay. HeLa-ACE2 cells were seeded in the assay-ready plates at 1.6×10^3 cells per well in assay medium, and plates were incubated for 24 hours at 37 °C with 5% CO₂. To assess cell viability, the Image-iT DEAD Green reagent (Thermo Fisher Scientific, I10291) was used according to the manufacturer's instructions. Cells were fixed with 4% PFA and counterstained with DAPI. Fixed cells were imaged using the ImageXpress Micro Confocal High-Content Imaging System (Molecular Devices) with a $\times 10$ objective, and total live cells per well quantified in the acquired images using the Live Dead Application Module (MetaXpress).

Data analysis of the compound screening results

The in vitro infection assay and the host cell cytotoxicity counterscreen data were uploaded to Genedata Screener, version 16.0. Data were normalized to neutral (DMSO) minus inhibitor controls (2.5 μ M remdesivir for antiviral effect and 10 μ M puromycin for infected host cell toxicity). For the uninfected host cell cytotoxicity counterscreen, 10 μ M puromycin (Sigma-Aldrich) was used as a positive control. For dose–response experiments, compounds were tested in technical triplicates, and dose curves were fitted with the four-parameter Hill equation. Replicate data were analyzed using median condensing. The full dataset is provided in Supplementary Dataset 1.

Pseudoviral entry assay

To measure SARS-CoV-2 viral infectivity, we performed pseudoviral entry assays as previously described³¹. In brief, HEK293T cells were transiently co-transfected with MLV-gag/pol, MLV-CMV-luciferase plasmid and SARS-CoV-2 spike (D614) or VSV-G plasmid. Two days later, supernatants containing pseudotyped virus particles were collected. To assay for pseudoviral entry, HeLa-ACE2 cells were seeded in 96-well plates at 10,000 cells per well (PerkinElmer, 6005680). One day later, cells were incubated with diluted pseudovirus. After 48 hours to allow for viral transduction, cells were lysed and assayed for luciferase activity by Steady-Glo (Promega, E2510) according to the manufacturer's instructions. Luminescence was quantified using a Luminoskan Ascent plate reader (Thermo Fisher Scientific). To assess the ability of NMT5 to reduce viral infection in human-ACE2 cells with SARS-CoV-2 variants, lenti-SARS-CoV-2 N501Y spike, SARS-CoV-2 K417N, E484K and N501Y spike and VSV-G pseudoviral particles were obtained from the Rhode Island Hospital lentivirus construct core⁵⁹, or lenti-SARS-CoV-2 Delta and Omicron variant pseudoviral particles were obtained from PBS Bioscience (78215 and 78348, respectively). SARS-CoV-2 variant preparations were diluted in assay media and added at 4.0×10^6 TU/ 1×10^4 or 1.5×10^2 TU/ 1×10^4 cells (for Delta variant), or 9×10^2 TU/ 1×10^4 cells (for Omicron variant), in the presence or absence of 20 μ M NMT5. Plates were centrifuged at 600g for 1 hour at room temperature, and then cells were incubated at 37 °C in a 5% CO₂ incubator. After 48 hours to allow for viral transduction, cells were lysed and assayed for luciferase activity by Steady-Glo. Luminescence was quantified using a Luminoskan Ascent plate reader.

PK testing and analysis

Golden Syrian hamsters (110–150 g, $n = 3$ for each compound) were dosed by oral gavage at 10 mg kg⁻¹. Blood samples were obtained at 30 minutes and at 1, 3, 7, 24, 32 and 48 hours. The blood samples were collected in BD Vacutainers (BD, 366664) containing sodium heparin and centrifuged. The processed plasma samples were stored at -20 °C until high-performance liquid chromatography–tandem mass spectrometry (HPLC–MS/MS) analysis. Animals were then sacrificed, and lung and kidney tissues were harvested for biotin switch analysis for SNO-ACE2. To quantify the test compound in the collected plasma samples, a plasma calibration curve was generated by spiking aliquots of drug-free plasma with the test compound at the specified concentration levels. Spiked and collected plasma samples were treated with an aliquot of acetonitrile containing a known concentration of an internal standard (IS). The extraction solvent was analyzed on an Agilent 1100 LC mated to an AB Sciex 4000 Q TRAP MS. Separation of the analytes was achieved by using a Phenomenex Kinetex EVO C18 50 \times 2.1-mm column (Phenomenex, 00B-4633-AN) and a mobile phase consisting of (A) 0.1% formic acid in water and (B) 0.1% formic acid in acetonitrile. The LC gradient consisted of a 0.5 ml min⁻¹ flow rate starting at 100% of (A). The LC gradient then ramped to 90% (B) over 0.1 minutes and held for 2.5 minutes. The gradient reverted to 100% (A) over 0.1 minute and allowed for 2 minutes of re-equilibration time. Ionization spray voltage was set to 4,000, with the source temperature set at 400 °C. Analytes were monitored by multiple reaction monitoring (MRM) in positive ionization mode. Peak areas were recorded, and the concentrations of the test compound in the unknown plasma samples were quantified by the calibration curve using Sciex Analyst software (PE Sciex). Phoenix WinNonLin 8.1 software (Certara) was used in NCA mode to determine the PK parameters from the LC–MS/MS measured values. NMT5 PK analysis was performed by 'serial sampling' where we followed the PK of the drug in each individual animal (animals 71, 73 and 75) and then averaged those PK values. We took this approach because all the animals had values for the full time course available, as detailed in Supplementary Dataset 2. For NMT3 PK, the 'sparse sampling' procedure was used to account for plasma concentrations from animals that did not have a full time course profile available (animals 372–374), in part due to the short half-life and rapid metabolism to the hydroxylated form with

release of the nitrate group, as detailed in Supplementary Dataset 3. The differences in methodology results in 'serial sampling' averaging the PK values and 'sparse sampling' averaging the concentrations were used to determine the PK values. Sparse sampling was also necessary because tissue samples were obtained at two of the timepoints (1 hour and 24 hours), so the study parameters had to be modified. Additionally, both parent drug (NMT3) and metabolite were detected, making the samples sparser. Summary PK data are shown in Supplementary Table 1, and the full datasets are provided in Supplementary Dataset 2 (for NMT5) and Supplementary Dataset 3 (for NMT3).

Syrian hamster COVID-19 model

Eight-week-old golden Syrian hamsters (110–150 g, Charles River Laboratories) were challenged with a dose of 1×10^5 or 1×10^6 plaque-forming units (PFU) of SARS-CoV-2 (USA-WA1/2020) by intranasal administration in a volume of 100 μ l of DMEM as previously described³¹. For the experiments shown, the hamsters were subsequently administered via oral gavage either vehicle or the aminoadamantane nitrate candidate drugs NMT3 or NMT5 in a volume of 500 μ l, with the initial dose timed for delivery right after challenge with SARS-CoV-2 and a second dose administered 12 hours later. At 2 days and 5 days after infection, lung tissue was collected for assessing viral titers and histology as described³¹. All animal experiments were approved by the Scripps Research Institute Animal Care and Use Committee.

Plaque assay for SARS-CoV-2 viral titers

SARS-CoV-2 titers were measured 2 days and 5 days after infection by homogenizing hamster lungs in DMEM 2% FBS using 100- μ m cell strainers (Myriad, 2825-8367). Homogenized lungs were titrated 1:10 over six steps and layered over Vero cells. After 1 hour of incubation at 37 °C, a 1% methylcellulose in DMEM overlay was added, and the cells were incubated for 3 days at 37 °C. Cells were then fixed with 4% PFA, and plaques were counted by crystal violet staining and expressed as PFU. PFU after treatment with NMT3 was statistically equal to that of vehicle control.

Lung histology and immunohistochemistry

Lung tissue from golden Syrian hamsters was stored in zinc formalin for >72 hours. The tissue was processed for paraffin embedding, and sections cut at a thickness of 5 μ m. The tissue was then stained with hematoxylin and eosin (H&E). The slides were scanned at $\times 20$ using an Aperio AT2 whole slide scanner. For immunohistochemistry, lung sections were fixed with 4% PFA for 15 minutes and washed three times with PBS. Sections were blocked with 3% BSA and 0.3% Triton X-100 in PBS for 30 minutes. Sections were incubated with primary antibody in blocking solution overnight at 4 °C and then washed with PBS. The appropriate Alexa Fluor 488-conjugated (Thermo Fisher Scientific, A21206) and Alexa Fluor 555-conjugated (Thermo Fisher Scientific, A31570) secondary antibodies were used at 1:500, plus Hoechst 33342, trihydrochloride and trihydrate dye (1:1,000, Thermo Fisher Scientific, H3570) to visualize nuclei, for 1 hour at room temperature. Primary antibodies and dilutions were as follows: mouse anti-TNF α (5 μ g ml⁻¹, Abcam, ab1793) and rabbit anti-macrophage inflammatory protein 1 α (MIP-1 α)/CCL3 + CCL3L1 (1:250, Abcam, ab259372). Slides were imaged using a C2 confocal microscope (Nikon) in a masked fashion. For quantification of lung injury, pathology scores were applied based on the percentage of interstitial hemorrhage and cytokines present using the following criteria: (0) normal; (1) less than 10% of tissue affected; (2) 10–25% affected; (3) 26–50% affected; and (4) more than 50% affected, similar to the scoring system used previously for COVID-19 models⁶⁰.

Patch-clamp analysis of SARS-CoV-2 E protein viroporin ion channel activity

Using the patch-clamp technique, we recorded whole-cell currents from untransfected HEK293T cells and cells transfected with

SARS-CoV-2 E protein. Cells were recorded at room temperature in HEPES-supplemented HBSS with the following composition (in mM): NaCl 138, KCl 5.3, KH_2PO_4 0.4, Na_2HPO_4 0.3, NaHCO_3 4.2, MgCl_2 0.5, MgSO_4 0.4, CaCl_2 2.0, D-glucose 5.6 and HEPES 10; pH 7.4, osmolality 300 mOsm. Patch pipettes were filled with an intracellular pipette solution composed of (in mM): 113 K-gluconate, 6 KCl, 4.6 MgCl_2 , 1.1 CaCl_2 , 10 HEPES, 10 EGTA, 4 $\text{Na}_2\text{-ATP}$, 0.4 $\text{Na}_2\text{-GTP}$, pH adjusted to 7.3 with KOH; osmolality 291 mOsm. Whole-cell currents were recorded using Clampex software (Molecular Devices) on a computer-controlled patch-clamp amplifier (Multiclamp 700B, Molecular Devices) and analyzed with Clampfit software (Molecular Devices). Traces were filtered at 2 kHz and sampled at 20 kHz. Drugs were dissolved in water and stored as 100 mM stocks at -20°C . During experiments, drugs were dissolved in extracellular solution and tested at concentrations of 5 μM and 10 μM . HEK293T cells were plated on 12-mm-diameter glass coverslips coated with a mixture of rat tail type I collagen and poly-D-lysine. For transient expression in HEK293T cells, we used a transfection reagent (FuGENE HD, Promega) to co-transfect plasmids containing cDNAs for SARS-CoV-2 E protein (pGBW-m4133502, Addgene) and green fluorescent protein (GFP) at a ratio of 1:0.1 (0.5:0.05 μg per well, respectively).

SNO-ACE2 targeting assay via E protein viroporin channel

SARS-CoV-2 E plasmid was transiently transfected into HEK293-spike cells with Lipofectamine 2000 (controls received Lipofectamine 2000 vehicle alone). One day later, cells were harvested by tapping the plate in pre-warmed PBS. These cells were then added onto pre-plated HeLa-ACE2 cells in the presence or absence of NMT5. After 30 minutes, all cells were collected and subjected to biotin switch assay and immunoblotting with anti-ACE2 antibody to assess the levels of SNO-ACE2 and total input ACE2.

Quantification and statistical analysis

A power analysis of our prior data was used to determine the number of replicates needed for statistical purposes. The number of replicates or experiments is indicated in the individual figure legends. Data are expressed as mean \pm s.e.m. In general, for multiple comparisons on data with a normal distribution, differences between experimental groups were evaluated using an ANOVA followed by a post hoc Tukey's or Fisher's least significant difference (LSD) test. For comparison between two groups, a Student's *t*-test (for normally distributed data) or a non-parametric Mann-Whitney *U*-test (for data not known to be normally distributed) was employed. Additionally, for the statistical assessment of lung pathology in the Syrian hamster model of COVID-19, a Fisher's exact test with a 2×2 contingency table was used. *P* values less than 0.05 were considered significant. Statistical analyses were performed using GraphPad Prism software.

Reporting summary

Further information on research design is available in the Nature Research Reporting Summary linked to this article.

Data availability

All data are available in the main text or the supplementary materials. All plasmids generated in this study are available from S.A.L. under a material transfer agreement with the Scripps Research Institute. The structure data for ACE2 protein is available at <https://www.rcsb.org/structure/6m17> (PDB ID: 6M17). Source data are provided with this paper.

References

42. Li, W. et al. Angiotensin-converting enzyme 2 is a functional receptor for the SARS coronavirus. *Nature* **426**, 450–454 (2003).
43. Uehara, T. et al. S-nitrosylated protein-disulphide isomerase links protein misfolding to neurodegeneration. *Nature* **441**, 513–517 (2006).

44. Ghatak, S. et al. Mechanisms of hyperexcitability in Alzheimer's disease hiPSC-derived neurons and cerebral organoids vs isogenic controls. *eLife* **8**, e50333 (2019).
45. He, L., Diedrich, J., Chu, Y. Y. & Yates, J. R. III Extracting accurate precursor information for tandem mass spectra by RawConverter. *Anal. Chem.* **87**, 11361–11367 (2015).
46. Xu, T. et al. ProLuCID: an improved SEQUEST-like algorithm with enhanced sensitivity and specificity. *J. Proteom.* **129**, 16–24 (2015).
47. Tabb, D. L., McDonald, W. H. & Yates, J. R. III DTASelect and Contrast: tools for assembling and comparing protein identifications from shotgun proteomics. *J. Proteome Res.* **1**, 21–26 (2002).
48. Peng, J., Elias, J. E., Thoreen, C. C., Licklider, L. J. & Gygi, S. P. Evaluation of multidimensional chromatography coupled with tandem mass spectrometry (LC/LC-MS/MS) for large-scale protein analysis: the yeast proteome. *J. Proteome Res.* **2**, 43–50 (2003).
49. Vanommeslaeghe, K., Raman, E. P. & MacKerell, A. D. Jr. Automation of the CHARMM General Force Field (CGenFF) II: assignment of bonded parameters and partial atomic charges. *J. Chem. Inf. Model.* **52**, 3155–3168 (2012).
50. Vanommeslaeghe, K. & MacKerell, A. D. Jr. Automation of the CHARMM General Force Field (CGenFF) I: bond perception and atom typing. *J. Chem. Inf. Model.* **52**, 3144–3154 (2012).
51. Yu, W., He, X., Vanommeslaeghe, K. & MacKerell, A. D. Jr. Extension of the CHARMM general force field to sulfonyl-containing compounds and its utility in biomolecular simulations. *J. Comput. Chem.* **33**, 2451–2468 (2012).
52. Casares, D., Escriba, P. V. & Rossello, C. A. Membrane lipid composition: effect on membrane and organelle structure, function and compartmentalization and therapeutic avenues. *Int. J. Mol. Sci.* **20**, 2167 (2019).
53. van Meer, G., Voelker, D. R. & Feigenson, G. W. Membrane lipids: where they are and how they behave. *Nat. Rev. Mol. Cell Biol.* **9**, 112–124 (2008).
54. Phillips, J. C. et al. Scalable molecular dynamics on CPU and GPU architectures with NAMD. *J. Chem. Phys.* **153**, 044130 (2020).
55. Huang, J. et al. CHARMM36m: an improved force field for folded and intrinsically disordered proteins. *Nat. Methods* **14**, 71–73 (2017).
56. Guvench, O., Hatcher, E. R., Venable, R. M., Pastor, R. W. & MacKerell, A. D. CHARMM additive all-atom force field for glycosidic linkages between hexopyranoses. *J. Chem. Theory Comput.* **5**, 2353–2370 (2009).
57. McGibbon, R. T. et al. MDTraj: a modern open library for the analysis of molecular dynamics trajectories. *Biophys. J.* **109**, 1528–1532 (2015).
58. Humphrey, W., Dalke, A. & Schulten, K. VMD: visual molecular dynamics. *J. Mol. Graph.* **14**, 27–38 (1996).
59. Zhou, L. et al. MEK inhibitors reduce cellular expression of ACE2, pERK, pRb while stimulating NK-mediated cytotoxicity and attenuating inflammatory cytokines relevant to SARS-CoV-2 infection. *Oncotarget* **11**, 4201–4223 (2020).
60. Shapira, T. et al. A TMPRSS2 inhibitor acts as a pan-SARS-CoV-2 prophylactic and therapeutic. *Nature* **605**, 340–348 (2022).

Acknowledgements

We thank D. Nemazee (Scripps Research Institute) for providing HeLa-ACE2 cells and plasmids for pseudovirus. This work was supported, in part, by National Institutes of Health (NIH) grants RF1 AG057409, R01 AG056259, R01 DA048882, R35 AG071734 and DP1 DA041722 (to S.A.L.), R01 AG061845, R61 NS122098 and RF1 NS123298 (to T.N.), UM1 A1144462 (to D.R.B.) and P41 GM103533 (to J.R.Y.), HOPE T32 training grant T32AI007384 (to L.N.C.); California Institute for Regenerative Medicine grant DISC2 COVID19-11811;

COVID-19 awards from Fast Grants (to S.A.L.); and grants from the Bill & Melinda Gates Foundation, OPP1107194 (to Calibr) and INV-004923 (to I.A.W). The molecular dynamics simulations were supported by NIH R01 GM132826, National Science Foundation (NSF) RAPID (MCB-2032054), an award from RCSA Research Corporation, a UC San Diego Moores Cancer Center 2020 SARS-CoV-2 seed grant (to R.E.A.) and the Interfaces Graduate Training Program, NIH T32 EB009380 (to M.A.R). We thank the Texas Advanced Computing Center Frontera team and acknowledge computer time made available through a Director's Discretionary Allocation (made possible by NSF award OAC-1818253). We also thank O. Liang of the Lentivirus Core of the COBRE Center for Stem Cells and Aging at Brown University, supported by NIH P20 GM119943.

Author contributions

S.A.L. conceived, designed and supervised the execution of the entire project. C.-K.O., T.N. and S.A.L. formulated the detailed research plans, interpreted experimental results and wrote the first draft of the manuscript. C.-K.O. performed most molecular and biochemical experiments, and X.Z. carried out biochemical experiments with mutant ACE2. N.B., S.R.M., N.S., D.R.B. and T.F.R. performed in vivo experiments with the Syrian hamster model. D.T. and L.N.C. performed immunohistochemistry on hamster lung tissue. J.P.-C., M.T. and S.G. performed electrophysiology experiments. M.A.B., A.J.R., A.K.W., V.C., A.K.G. and A.K.C. conducted compound screening and pharmacokinetic analyses. T.N., J.K.D. and J.R.Y. conducted mass spectrometry assays. M.A.R., F.L.K., L.C. and R.E.A. conducted molecular dynamics simulations. H.L. and I.A.W. produced recombinant ACE2 and helped write the structure-related aspects of the manuscript. C.-K.O. and S.A.L. wrote and compiled the initial manuscript, and C.-K.O., T.N., S.R.M., I.A.W., R.E.A., D.R.B., J.R.Y., T.F.R., A.K.C. and S.A.L. then reviewed and edited the manuscript.

Competing interests

The authors declare that S.A.L. is an inventor on patents for the use of memantine and various aminoadamantane nitrate compounds for neurodegenerative and neurodevelopmental disorders. He is also an inventor on composition of matter patents and use patents for aminoadamantane nitrate compounds in treating COVID-19 and other viral diseases. Per Harvard University guidelines, S.A.L. participates in a royalty-sharing agreement with his former institution, Boston Children's Hospital/Harvard Medical School, which licensed the drug memantine (Namenda) to Forest Laboratories/Actavis/Allergan/AbbVie for use in dementia. The aminoadamantane nitrate compounds have been licensed to EuMentis Therapeutics. C.B. is a chemist employed at EuMentis Therapeutics. The other authors declare no financial conflicts of interest relevant to this publication.

Additional information

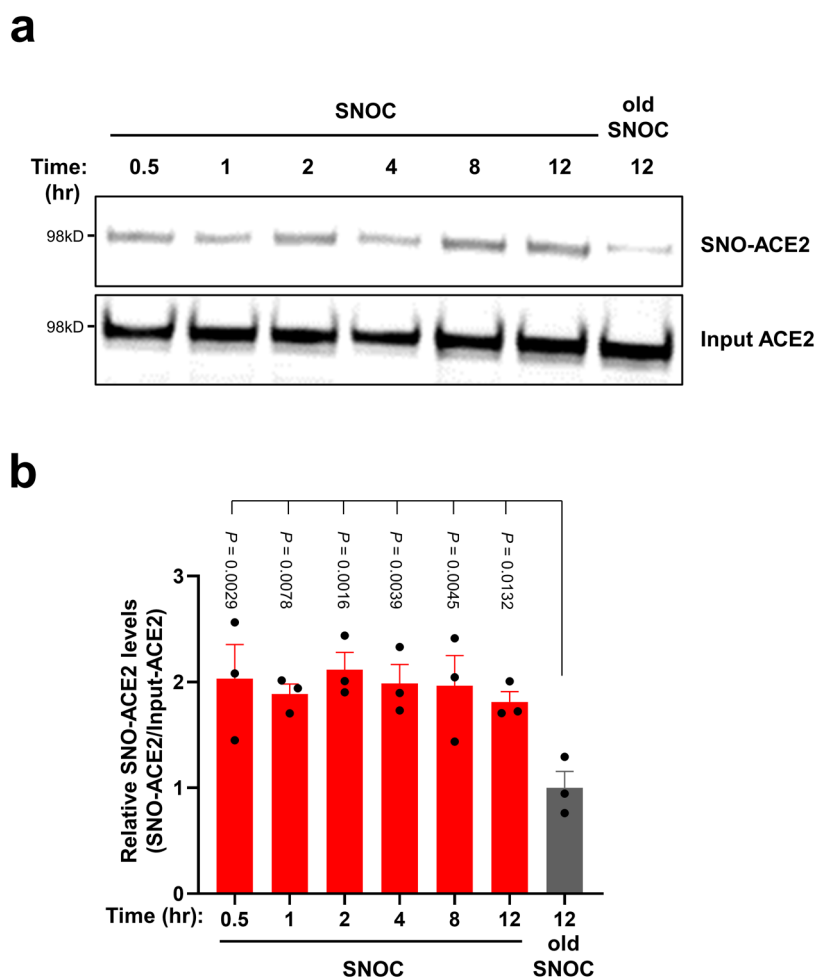
Extended data is available for this paper at <https://doi.org/10.1038/s41589-022-01149-6>.

Supplementary information The online version contains supplementary material available at <https://doi.org/10.1038/s41589-022-01149-6>.

Correspondence and requests for materials should be addressed to Stuart A. Lipton.

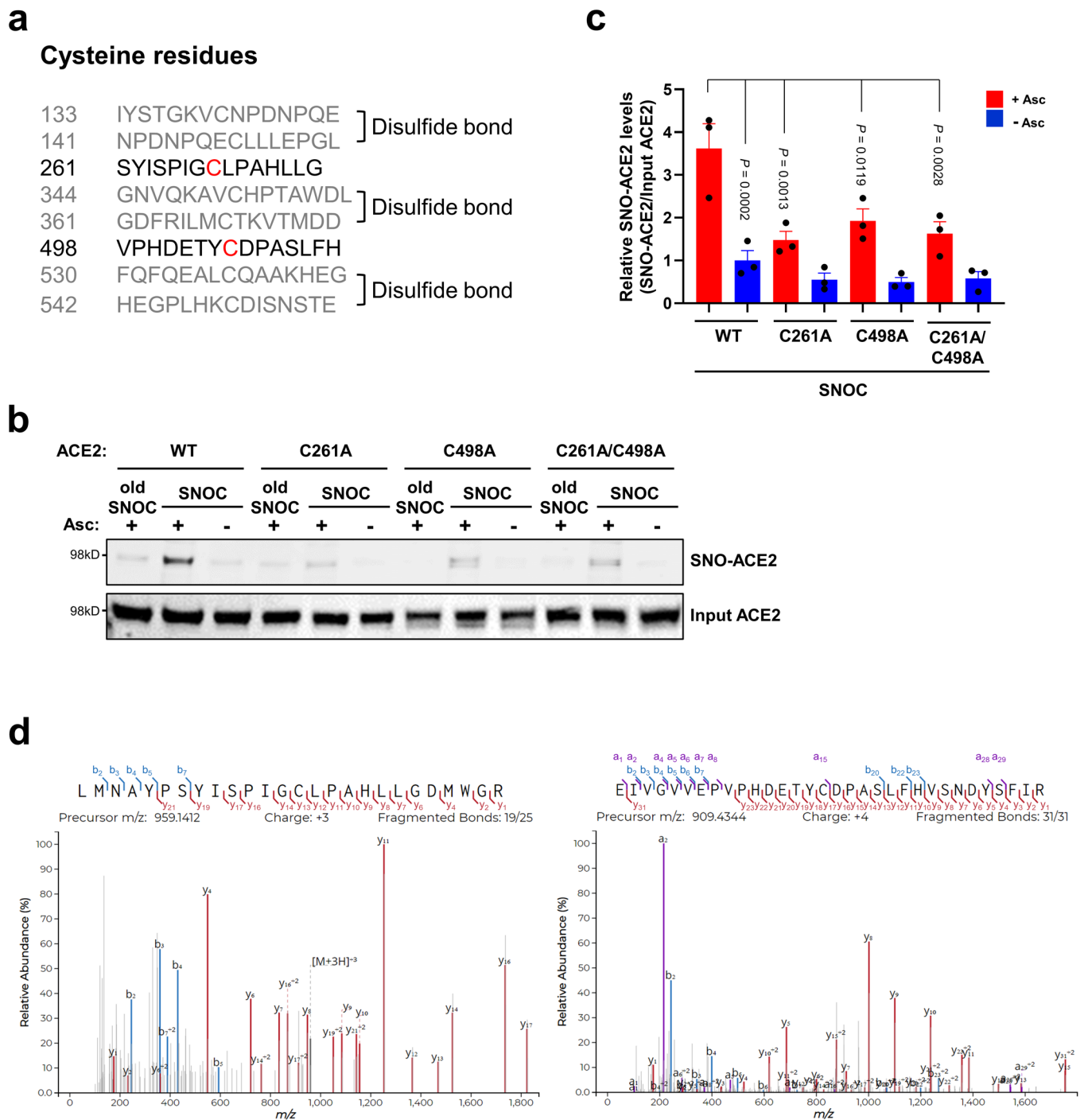
Peer review information *Nature Chemical Biology* thanks Francesco Galli, Yasuo Mori and the other, anonymous, reviewer(s) for their contribution to the peer review of this work.

Reprints and permissions information is available at www.nature.com/reprints.

**Extended Data Fig. 1 | S-Nitrosylation of ACE2 persists for at least 12 hours.**

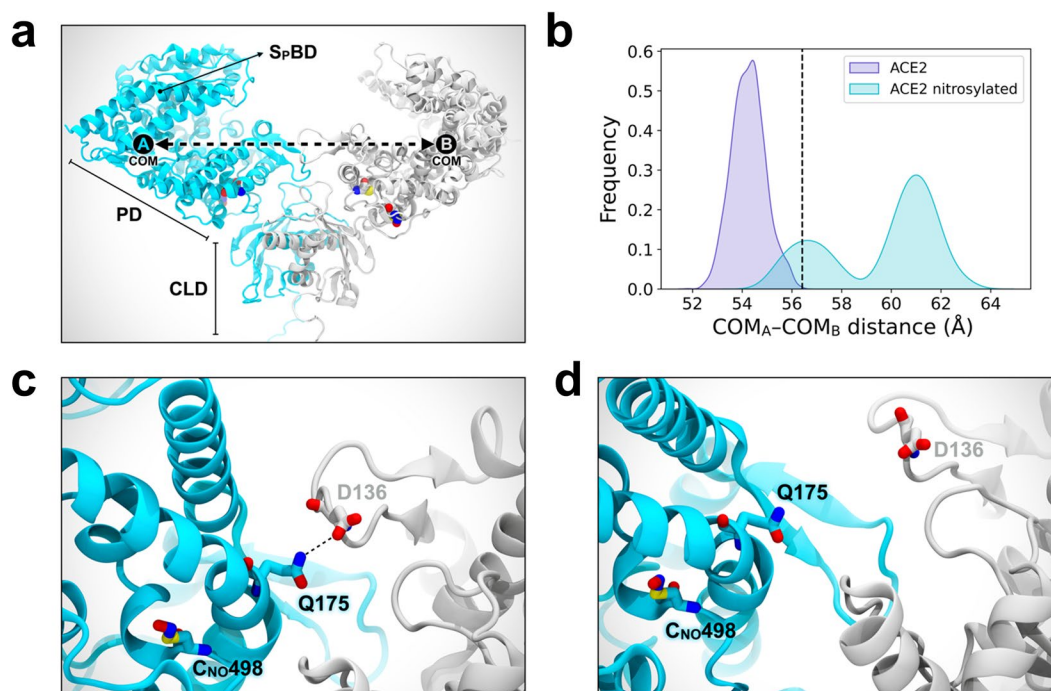
a, HeLa-ACE2 cells were exposed to 100 μ M SNOC; 30 min later the cells were incubated in serum free medium for the time periods indicated. Cell lysates were then subjected to biotin-switch assay to assess protein S-nitrosylation, which

was detected by immunoblotting with anti-ACE2 antibody. **b**, Ratio of SNO-ACE2/input ACE2 protein. Data are mean + s.e.m. by one-way ANOVA with Fisher's LSD multiple comparisons. $n = 3$ biological replicates.



Extended Data Fig. 2 | Identification of cysteine residues in ACE2 that are S-nitrosylated. **a**, List of human ACE2 peptides (± 7 amino acid residues flanking a cysteine residue); gray: peptides involved in disulfide bond formation; black: peptides containing a free cysteine thiol (red) that could potentially be S-nitrosylated. **b**, HEK293T cells were transiently transfected with plasmids containing human WT ACE2 or cysteine mutant ACE2 (C261A, C498A, or C261/498A). One day after transfection, cells were exposed to 100 μ M SNOC.

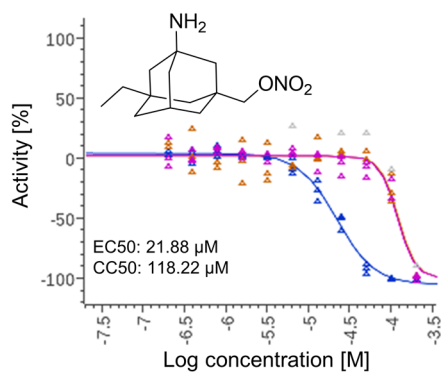
After 20 minutes, cells were subjected to biotin-switch assay. Absence of ascorbate (Asc⁻) served as a negative control. **c**, Ratio of SNO-ACE2/input ACE2. Data are mean \pm s.e.m. by two-way ANOVA with Tukey's multiple comparisons. $n = 3$ biological replicates. **d**, HEK293T cells expressing ACE2 were exposed to SNOC and subjected to biotin switch. The peptides were eluted by reduction for subsequent detection by LC-MS/MS. Representative MS/MS spectra of detected peptides from human ACE2 containing Cys²⁶¹ (left) or Cys⁴⁹⁸ (right) are shown.



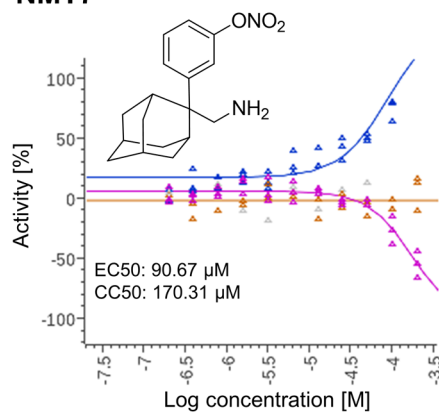
Extended Data Fig. 3 | Molecular dynamics simulation of S-nitrosylation of ACE2. **a**, Molecular representation of the S-nitrosylated-ACE2/RBD model upon transient detachment at the level of the peptidase domain dimeric interface. SNO-Cys261 and SNO-Cys498 are shown with Van der Waals spheres. The black dots indicate qualitative placement of centers of mass (COM) for each ACE2 protomer, and the dashed arrow represents the distance between COMs. Spike's RBDs and N-glycans, which were included in the simulation, are hidden for image clarity. SpBD, Spike binding domain; CLD, collectrin-like domain; PD, peptidase domain. **b**, Distribution of the distance between COMs from molecular dynamics

simulations of WT ACE2/RBD (purple) vs. nitrosylated-ACE2/RBD (cyan). Dashed black line at approximately 56.5 Å indicates the reference distance between COMs calculated from the cryo-EM structure (PDB: 6M17). S-Nitrosylated-ACE2/RBD shows an overall larger distance between COMs with a bimodal distribution. **c**, Close-up image illustrating Q175A to D136B interaction present in starting conformations of the S-nitrosylated-ACE2 system. **d**, Close-up image illustrating the disruption of the interaction between Q175A and D136B occurring along the dynamics of the S-nitrosylated-ACE2 system.

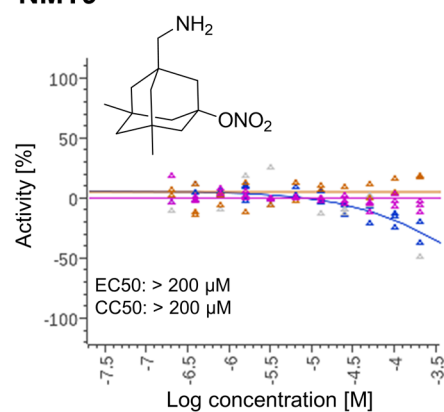
NMT2



NMT7



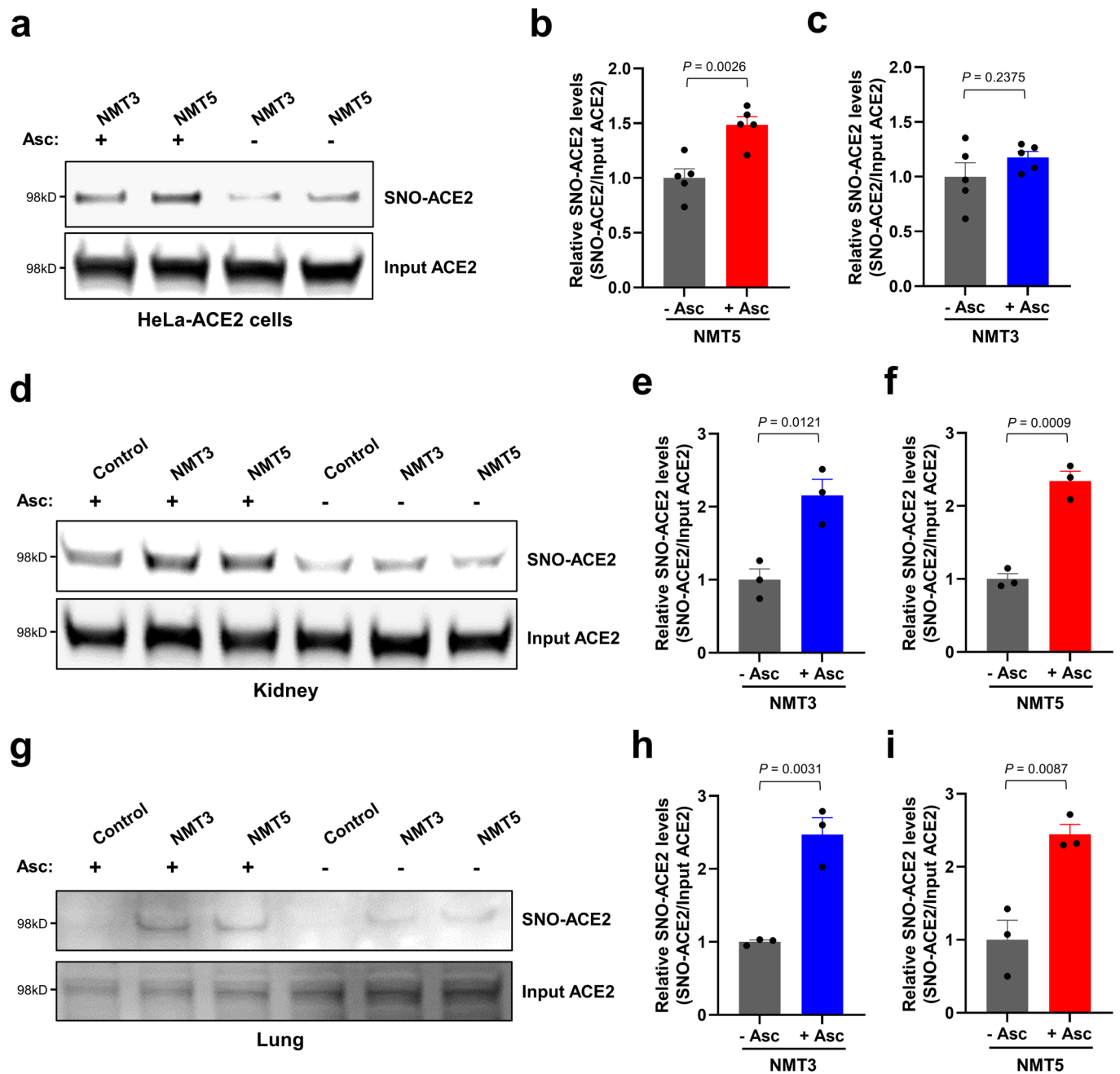
NMT9



- Treatment compounds: % Infected (MultiWaveScoring)
- Treatment compounds: Total Cells (MultiWaveScoring)
- Treatment compounds uninfected HeLa-ACE2: Live Cells (LiveDead)

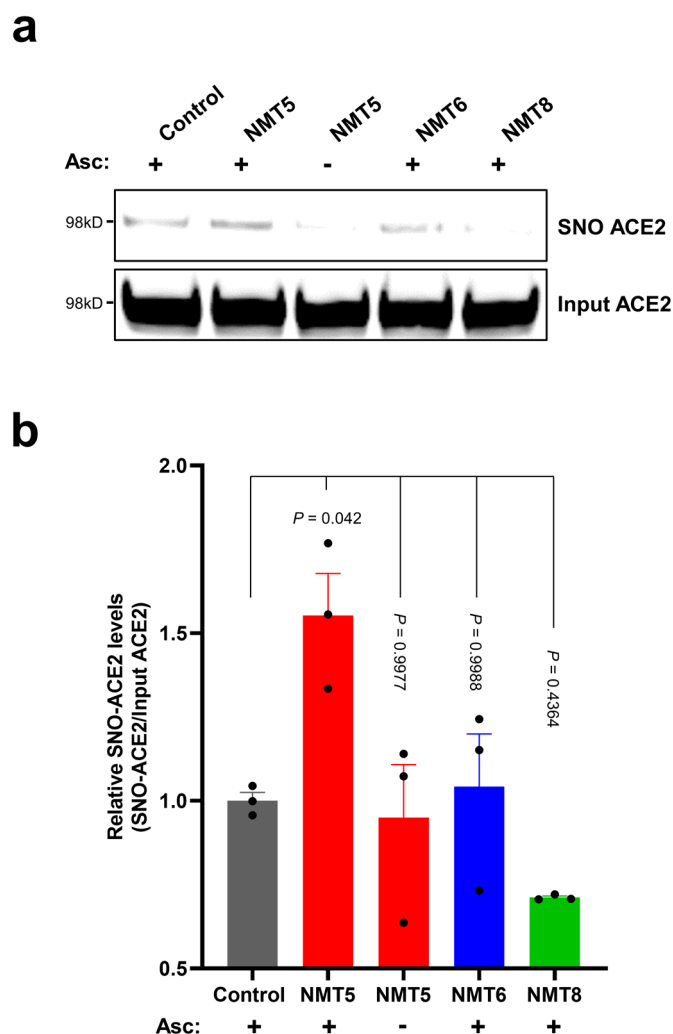
Extended Data Fig. 4 | Dose-response of drugs screened against SARS-CoV-2 infection. Dose-response curves showing the EC₅₀ of each compound against SARS-CoV-2 (% infected cells, blue), total cell counts (orange) in the infection

experiment and the CC₅₀ for uninfected host cell toxicity (magenta), as assessed in HeLa-ACE2 cells. See also Supplementary Dataset 1 for full dataset. Continued from Fig. 2.



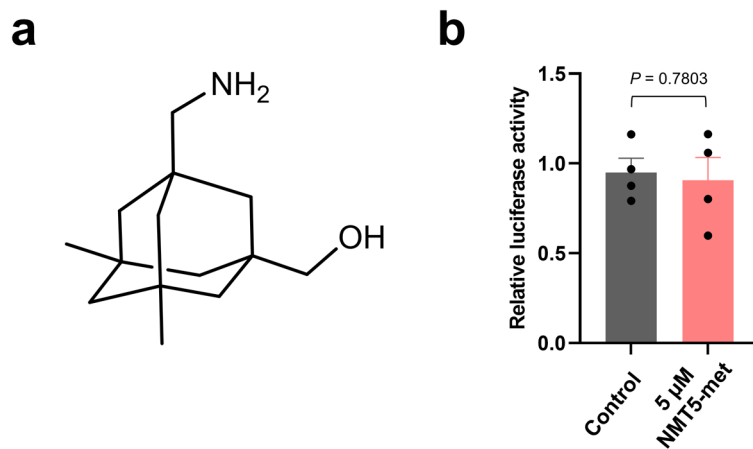
Extended Data Fig. 5 | NMT5 S-nitrosylates ACE2 *in vitro* and *in vivo*. **a**, Detection of SNO-ACE2 *in vitro*. HeLa-ACE2 cells were exposed to 10 μ M NMT3 or 5 μ M NMT5. After 1 h, cells were subjected to the biotin-switch assay in the presence or absence of ascorbate. SNO-ACE2 and input ACE2 were detected by immunoblotting with anti-ACE2 antibody. **b, c**, Ratio of SNO-ACE2/input ACE2. Data are mean \pm s.e.m. by two-tailed Student's *t* test. $n = 5$ biological replicates. **d–i**, Detection of SNO-ACE2 *in vivo*. Syrian hamsters received 10 mg/kg of NMT3

or of NMT5 by oral gavage and were sacrificed 48 h later. Kidney and lung tissues were subjected to biotin-switch assay in the presence or absence of ascorbate. Note that in some samples, low levels of SNO-ACE2 were observed in control tissue, suggesting endogenous S-nitrosylation of ACE2 may occur at low levels. Graphs show ratio of SNO-ACE2/input ACE2. Data are mean \pm s.e.m. by two-tailed Student's *t* test. $n = 3$ Syrian hamsters for each condition.



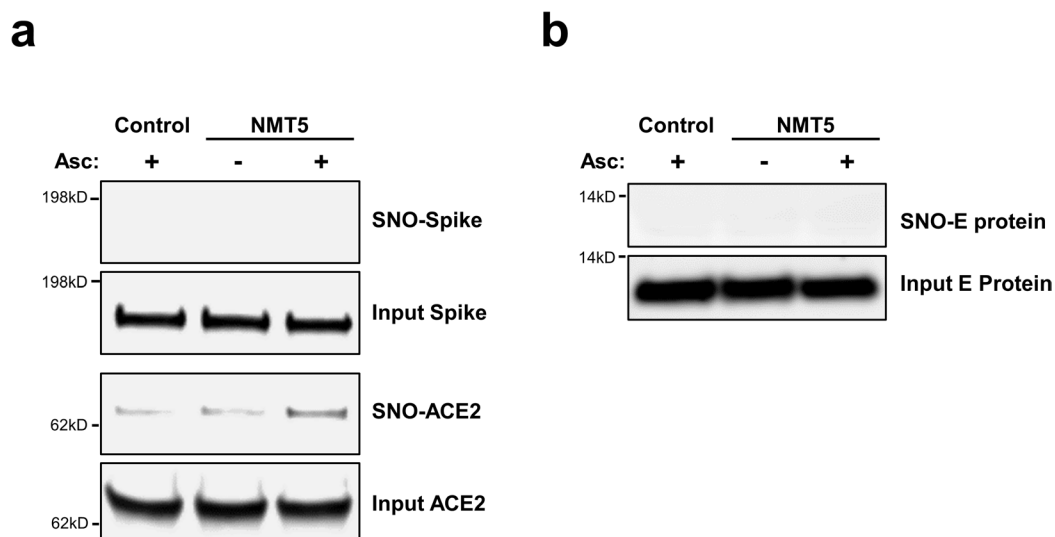
Extended Data Fig. 6 | Protein S-nitrosylation of ACE2 by NMT5. **a**, HeLa-ACE2 cells were treated with 10 μ M NMT5, NMT6, or NMT8. After 1 h, cell lysates were subjected to biotin-switch assay for protein S-nitrosylation, detected by

immunoblotting with anti-ACE2 antibody. The ascorbate minus (Asc-) sample served as a negative control. **b**, Ratio of SNO-ACE2/input ACE2 protein. Data are mean + s.e.m. by one-way ANOVA with Tukey's multiple comparisons. $n = 3$



Extended Data Fig. 7 | Critical role of nitro group of NMT5 suppressing SARS-CoV-2 infection on pseudovirus entry assay. **a**, Chemical structure of NMT5 metabolite (NMT5-met, lacking the nitro group). **b**, HeLa-ACE2 cells were incubated in the presence and absence of 5 μ M NMT5-met with SARS-CoV-2

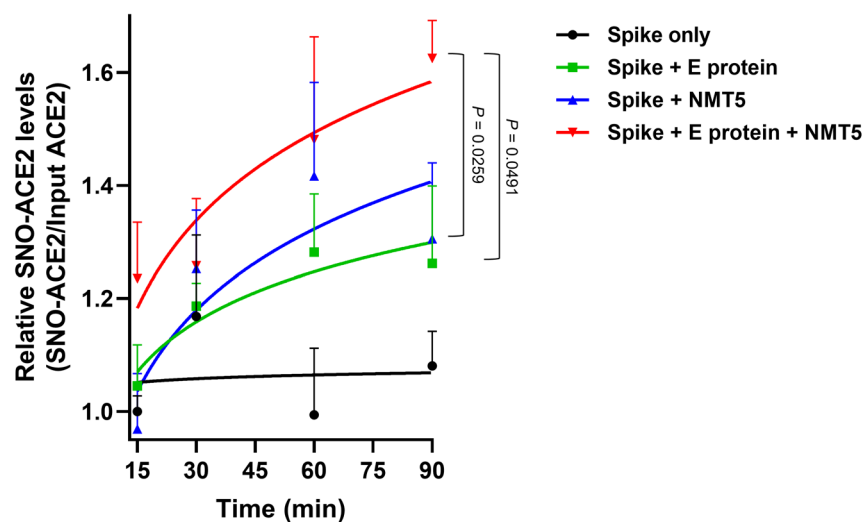
Spike (D614) pseudovirus particles. After 48 h, viral transduction efficiency was monitored by luciferase activity. Inhibitory activity was lost in the absence of the nitro group (compare with Fig. 3c,e). Data are mean + s.e.m. by two-tailed Student's *t* test. *n* = 4 biological replicates.



Extended Data Fig. 8 | Lack of S-nitrosylation of Spike protein and E protein.

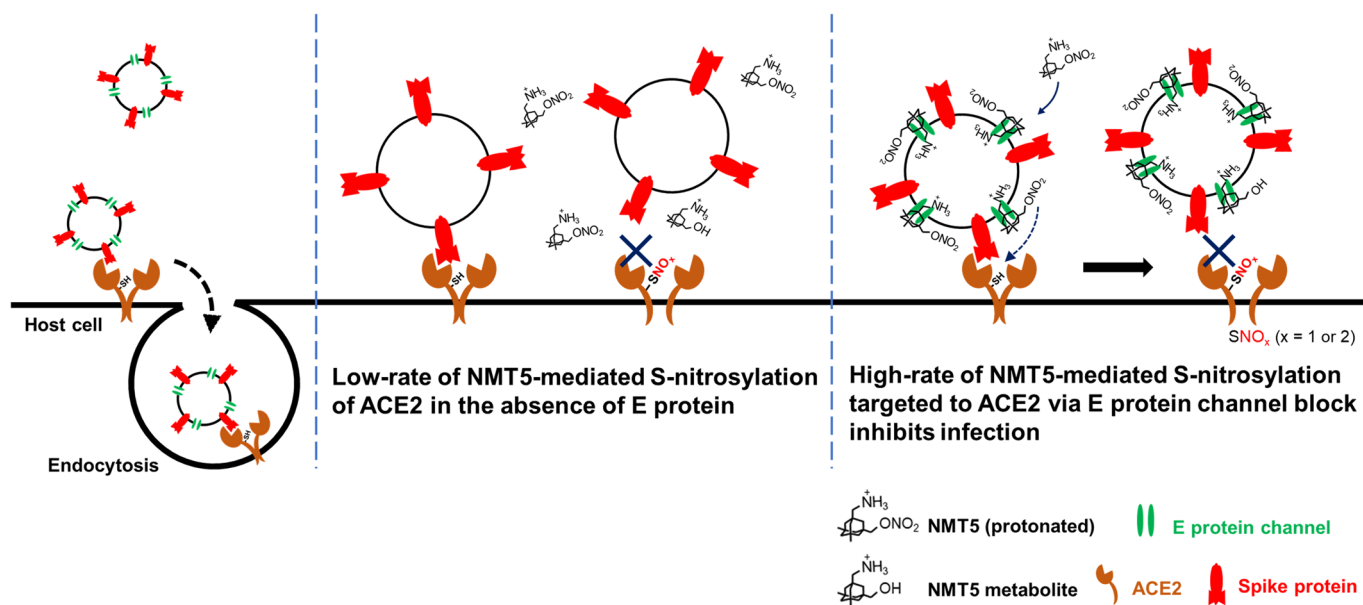
a, Purified recombinant SARS-CoV-2 Spike (S1 + S2) protein and ACE2 protein were exposed to 100 μ M SNOC; 30 min later, samples were subjected to biotin-switch assay in the presence or absence of ascorbate (Asc) to assess protein S-nitrosylation. $n = 3$ biological replicates. **b**, Lack of E protein S-nitrosylation

by NMT5. HA-tagged E protein plasmid was transiently transfected into HEK293 cells. One day after transfection, cells were exposed to 10 μ M NMT5. After 1 hour, the cells were harvested and subjected to biotin-switch assay in the presence or absence of ascorbate (Asc) to assess protein S-nitrosylation, which was detected by immunoblotting with anti-HA antibody. $n = 3$ biological replicates.



Extended Data Fig. 9 | Targeted S-nitrosylation of ACE2 by NMT5 in the presence of envelope (E) viroporin protein. Kinetic analysis of S-nitrosylation of ACE2. E protein plasmid was transiently transfected into HEK293 cells stably-expressing Spike protein cells. Subsequently, the cells were harvested and plated onto ACE2-expressing HeLa cells in the presence or absence of 20 μ M NMT5. At

the indicated timepoints, cells were subjected to biotin-switch assay. Ordinate shows ratio of SNO-ACE2/total input ACE2 protein above the baseline value, defined as 1.0. Data are mean + s.e.m. by two-way ANOVA with Fisher's LSD test. n = 5 biological replicates.



Extended Data Fig. 10 | Schematic of NMT5 targeting of SNO-ACE2 via SARS-CoV-2 E protein. S-Nitrosylation of ACE2 on the host cell inhibits SARS-CoV-2 entry and thus infection. Note that at physiological pH, the bridgehead amine of NMT5, like other aminoadamantanes, is generally protonated to NH_3^+ .

Reporting Summary

Nature Portfolio wishes to improve the reproducibility of the work that we publish. This form provides structure for consistency and transparency in reporting. For further information on Nature Portfolio policies, see our [Editorial Policies](#) and the [Editorial Policy Checklist](#).

Statistics

For all statistical analyses, confirm that the following items are present in the figure legend, table legend, main text, or Methods section.

n/a	Confirmed
<input type="checkbox"/>	<input checked="" type="checkbox"/> The exact sample size (n) for each experimental group/condition, given as a discrete number and unit of measurement
<input type="checkbox"/>	<input checked="" type="checkbox"/> A statement on whether measurements were taken from distinct samples or whether the same sample was measured repeatedly
<input type="checkbox"/>	<input checked="" type="checkbox"/> The statistical test(s) used AND whether they are one- or two-sided <i>Only common tests should be described solely by name; describe more complex techniques in the Methods section.</i>
<input checked="" type="checkbox"/>	<input type="checkbox"/> A description of all covariates tested
<input type="checkbox"/>	<input checked="" type="checkbox"/> A description of any assumptions or corrections, such as tests of normality and adjustment for multiple comparisons
<input type="checkbox"/>	<input checked="" type="checkbox"/> A full description of the statistical parameters including central tendency (e.g. means) or other basic estimates (e.g. regression coefficient) AND variation (e.g. standard deviation) or associated estimates of uncertainty (e.g. confidence intervals)
<input checked="" type="checkbox"/>	<input type="checkbox"/> For null hypothesis testing, the test statistic (e.g. F , t , r) with confidence intervals, effect sizes, degrees of freedom and P value noted <i>Give P values as exact values whenever suitable.</i>
<input type="checkbox"/>	<input checked="" type="checkbox"/> For Bayesian analysis, information on the choice of priors and Markov chain Monte Carlo settings
<input checked="" type="checkbox"/>	<input type="checkbox"/> For hierarchical and complex designs, identification of the appropriate level for tests and full reporting of outcomes
<input checked="" type="checkbox"/>	<input type="checkbox"/> Estimates of effect sizes (e.g. Cohen's d , Pearson's r), indicating how they were calculated

Our web collection on [statistics for biologists](#) contains articles on many of the points above.

Software and code

Policy information about [availability of computer code](#)

Data collection

Data analysis

For manuscripts utilizing custom algorithms or software that are central to the research but not yet described in published literature, software must be made available to editors and reviewers. We strongly encourage code deposition in a community repository (e.g. GitHub). See the Nature Portfolio [guidelines for submitting code & software](#) for further information.

Data

Policy information about [availability of data](#)

All manuscripts must include a [data availability statement](#). This statement should provide the following information, where applicable:

- Accession codes, unique identifiers, or web links for publicly available datasets
- A description of any restrictions on data availability
- For clinical datasets or third party data, please ensure that the statement adheres to our [policy](#)

All data are available in the main text or the supplementary materials. All plasmids generated in this study are available under a material transfer agreement with The Scripps Research Institute. The structure data of ACE2 protein is available at <https://www.rcsb.org/structure/6m17> (PDB 6M17).

Field-specific reporting

Please select the one below that is the best fit for your research. If you are not sure, read the appropriate sections before making your selection.

☒ Life sciences ☐ Behavioural & social sciences ☐ Ecological, evolutionary & environmental sciences

For a reference copy of the document with all sections, see [nature.com/documents/nr-reporting-summary-flat.pdf](https://www.nature.com/documents/nr-reporting-summary-flat.pdf)

Life sciences study design

All studies must disclose on these points even when the disclosure is negative.

Sample size	Sample sizes were chosen based on similar experiments previously published from which we could perform a Power Analysis. Additionally, for animal experiments, we used minimum numbers of hamsters that allowed us to obtain statistically meaningful results, in compliance with animal ethics regulations.
Data exclusions	No data were excluded.
Replication	The following experiments were repeated independently with similar results by indicated biological replicates: Fig. 1b (n=3), 1c (n=3), 1e (n=3), Fig. 3b (n=5), 3c (n=3 to 7), 3d (n=3), 3e (n=3), 3f (n=3), Fig. 4b (n=3), 4e (n=4), Fig. 5b (n=3), 5c (n=15), 5d (n=15), 5e (n=4), 5f (n=16), Fig. 6a (n=6), 6b (n=3), 6c (n=8), 6f (n=9); Extended Data Fig. 1b (n=3), Extended Data Fig. 2b (n=3), Extended Data Fig. 5b (n=5), 5c (n=5), 5e (n=3), 5f (n=3), 5h (n=3), 5i (n=3), Extended Data Fig. 6b (n=3), Extended Data Fig. 7b (n=4), Extended Data Fig. 8a (n=3), 8b (n=3), and Extended Data Fig. 9 (n=5)
Randomization	All samples were randomly chosen and assigned to different experimental groups.
Blinding	For microscopic experiments, investigators were blinded during data collection and analysis. In addition, for the majority of the immunoblot results, we used automated methods (Li-Cor image scanner, quantification of fluorescence images) to quantify the data.

Reporting for specific materials, systems and methods

We require information from authors about some types of materials, experimental systems and methods used in many studies. Here, indicate whether each material, system or method listed is relevant to your study. If you are not sure if a list item applies to your research, read the appropriate section before selecting a response.

Materials & experimental systems

n/a	Involved in the study
<input type="checkbox"/>	<input checked="" type="checkbox"/> Antibodies
<input type="checkbox"/>	<input checked="" type="checkbox"/> Eukaryotic cell lines
<input checked="" type="checkbox"/>	<input type="checkbox"/> Palaeontology and archaeology
<input type="checkbox"/>	<input checked="" type="checkbox"/> Animals and other organisms
<input checked="" type="checkbox"/>	<input type="checkbox"/> Human research participants
<input checked="" type="checkbox"/>	<input type="checkbox"/> Clinical data
<input checked="" type="checkbox"/>	<input type="checkbox"/> Dual use research of concern

Methods

n/a	Involved in the study
<input checked="" type="checkbox"/>	<input type="checkbox"/> ChIP-seq
<input checked="" type="checkbox"/>	<input type="checkbox"/> Flow cytometry
<input checked="" type="checkbox"/>	<input type="checkbox"/> MRI-based neuroimaging

Antibodies

Antibodies used	The following commercial antibodies were used in this study: anti-ACE2 (Abcam, ab15348, Lot #GR3344201-1; Proteintech, 21115-1-AP, Lot #00087165), anti-TMPRSS2 (Santa Cruz, sc-515727, Lot #D2420), anti-SARS-CoV-2 spike protein (Abcam, ab275759, Lot #GR3360068-6; Sino Biological, 40150-R007, Lot #MA14FE2702-B), anti-TNFα (Abcam, ab1793, Lot #GR3354381-1), and anti- MIP-1α/CCL3+CCL3L1 (Abcam, ab259372, Lot #GR3371299-7), IR-dye 680LT-conjugated goat anti-mouse (Li-Cor, 926-68020, Lot #D10324-15), IR-dye 800CW-conjugated goat anti-rabbit (Li-Cor, 926-32211, Lot #D10831-15), Alexa Fluor 488-conjugated secondary antibody (Thermo Fisher Scientific, A21206, Lot #2045215), Alexa Fluor 555-conjugated secondary antibody (Thermo Fisher Scientific, A31570, Lot #1984063).
Validation	All antibodies used in this study were validated by the manufacturers via immunoblotting or immunocytochemistry. anti-ACE2 (https://www.abcam.com/ace2-antibody-ab15348.html , https://www.ptglab.com/products/ACE2-Antibody-21115-1-AP.htm) anti-TMPRSS2 (https://www.scbt.com/p/tmprrs4-antibody-a-3?gclid=Cj0KCQjw852XBhC6ARIsAJsFPN1BWbdnwwTvEjhKHQR1bGGWN7250JgADMcuVGl0twM4zCFONHPVUaAqTLEALw_wcB) anti-SARS-CoV-2 spike protein (https://www.abcam.com/sars-cov-2-spike-glycoprotein-s1-antibody-ab275759.html ; https://www.sinobiological.com/antibodies/cov-spike-40150-r007?gclid=Cj0KCQjw852XBhC6ARIsAJsFPN3kuEkvun0-sQZ458ghcW6bkjVZg_HngZtPhlV5qDK_fibWxHijxjAaAg2eEALw_wcB) anti-TNFα(https://www.abcam.com/tnf-alpha-antibody-52b83-ab1793.html) nti- MIP-1α/CCL3+CCL3L1 (https://www.abcam.com/macrophage-inflammatory-protein-1-alpha--ccl3--ccl3l1-antibody-epr23751-54-

ab259372.html)

IR-dye 680LT-conjugated goat anti-mouse (<https://www.licor.com/bio/reagents/irdye-680lt-goat-anti-mouse-igg-secondary-antibody>)

IR-dye 800CW-conjugated goat anti-rabbit (<https://www.licor.com/bio/reagents/irdye-800cw-goat-anti-rabbit-igg-secondary-antibody>)

Alexa Fluor 488-conjugated secondary antibody (<https://www.thermofisher.com/antibody/product/Donkey-anti-Rabbit-IgG-H-L-Highly-Cross-Adsorbed-Secondary-Antibody-Polyclonal/A-21206>)

Alexa Fluor 555-conjugated secondary antibody (<https://www.thermofisher.com/antibody/product/Donkey-anti-Mouse-IgG-H-L-Highly-Cross-Adsorbed-Secondary-Antibody-Polyclonal/A-31570>)

Eukaryotic cell lines

Policy information about [cell lines](#)

Cell line source(s)

Vero E6 cells (ATCC CRL-1586)

HEK293T (System Biosciences, LV900A-1)

HEK293-Spike cells (SARS-CoV-2 Spike (D614)-expressing 293 cells [293-SARS2-S cells, InvivoGen], 293-cov2-s)

HeLa-ACE2 cells were generated and provided by Dr. David Nemazzi (Science. 2020 Aug 7;369(6504):731-736)

Authentication

Vero E6 cells were authenticated by ATCC before the purchase.

HEK293T cells were authenticated by System Biosciences before the purchase.

HEK293-Spike cells were authenticated by InvivoGen before the purchase and validated by immunoblotting with anti-Spike protein antibody.

HeLa-Ace2 cells were authenticated in Science. 2020 Aug 7;369(6504):731-736 and validated by immunoblotting with anti-ACE2 antibody.

Mycoplasma contamination

All cell lines routinely tested negative for mycoplasma contamination.

Commonly misidentified lines
(See [ICLAC](#) register)

No commonly misidentified cell lines were used.

Animals and other organisms

Policy information about [studies involving animals](#); [ARRIVE guidelines](#) recommended for reporting animal research

Laboratory animals

Eight-week-old male Golden Syrian hamsters (110-150 gm) were used in this study.

Wild animals

No wild animals were used.

Field-collected samples

No field-collected samples were used.

Ethics oversight

All animal experiments were approved by The Scripps Research Institute Animal Care and Use Committee.

Note that full information on the approval of the study protocol must also be provided in the manuscript.